
PERGAMON

Journal of the Mechanics and Physics of Solids
49 (2001) 1361–1395

JOURNAL OF THE
MECHANICS AND
PHYSICS OF SOLIDS

www.elsevier.com/locate/jmps

Boundary layers in constrained plastic flow: comparison of nonlocal and discrete dislocation plasticity

J.Y. Shu[a], N.A. Fleck[b], E. Van der Giessen[c], A. Needleman[d,*]

[a] *TCAD Group, Avant! Corporation, Bayside Parkway, Fremont, CA 94538, USA*
[b] *Engineering Department, Cambridge University, Cambridge, CB2 1PZ, UK*
[c] *Delft University of Technology, Koiter Institute Delft, Mekelweg 2, 2628 CD Delft, Netherlands*
[d] *Division of Engineering, Brown University, Providence, RI 02912, USA*

Received 6 March 2000; received in revised form 12 September 2000; accepted 14 October 2000

Abstract

Simple shear of a constrained strip is analyzed using discrete dislocation plasticity and strain gradient crystal plasticity theory. Both single slip and symmetric double slip are considered. The loading is such that for a local continuum description of plastic flow the deformation state is one of homogeneous shear. In the discrete dislocation formulation the dislocations are all of edge character and are modeled as line singularities in an elastic material. Dislocation nucleation, the lattice resistance to dislocation motion and dislocation annihilation are incorporated into the formulation through a set of constitutive rules. A complementary solution that enforces the boundary conditions is obtained via the finite element method. The discrete dislocation solutions give rise to boundary layers in the deformation field and in the dislocation distributions. The back-extrapolated flow strength for symmetric double slip increases with decreasing strip thickness, so that a size effect is observed. The strain gradient plasticity theory used here is also found to predict a boundary layer and a size effect. Nonlocal material parameters can be chosen to fit some, but not all, of the features of the discrete dislocation results. Additional physical insight into the slip distribution across the strip is provided by simple models for an array of mode II cracks.

Keywords: B. Constitutive behavior; B. Crystal plasticity; A. Dislocations; B. Metallic materials

* Corresponding author. Tel.: +1-401-863-2863; fax: 1-401-863-1157.
E-mail address: needle@engin.brown.edu (A. Needleman).

0022-5096/01/$ - see front matter
PII: S0022-5096(00)00074-0

1. Introduction

In monophase metal single crystals, dislocations can generally glide long distances relatively unimpeded. Indeed, surface slip steps that result from dislocations propagating through the interior and exiting the lateral surfaces are evidence for this. The situation is different in the interior of a structural metal or a multi-phase material. Incoherent precipitates, grain boundaries and phase boundaries can provide strong obstacles to glide. Dislocations pile up at the boundaries and the stress field so induced tends to restrict further dislocation motion, giving rise to increased strength and, as noted by Petch (1953), a size effect. Hence, the constraining role of boundaries is an essential ingredient in accounting for the difference between the plastic properties of polycrystalline and layered material and those of monophase single crystals.

Indeed, predicting a size effect has provided the motivation for much recent work on nonlocal plasticity formulations. Classical theories of plasticity predict a size independent response. Nonlocal formulations include a material length scale, and thus permit size effects to be modeled, see for example Aifantis (1984), Acharya and Bassani (2000), Fleck and Hutchinson (1993, 1997), Shu and Fleck (1999), Gao et al. (1999), Busso et al. (2000), Ortiz et al. (2000), Huang et al. (2000) and Gurtin (2000). Very different nonlocal theoretical frameworks can give rise to size effects. For example, several of these theories involve higher-order boundary conditions, while in other theories gradient effects enter through an internal variable and only classical boundary conditions are imposed. The correctness of these various approaches can be decided through a comparison of their predictions with experiment or with predictions of a direct dislocation-based description of plastic flow. Such comparisons are just beginning to be carried out, Bassani et al. (2001).

The objective of this study is such a comparison for simple shear of a confined plastically deforming strip. The strip is comprised of a single crystal which is deforming in single slip or in symmetric double slip. For any classical elastic–plastic solid, the solution to the boundary value problem posed is a homogeneous deformation state. When this boundary value problem is solved using the discrete dislocation plasticity framework of Van der Giessen and Needleman (1995) and Cleveringa et al. (1997), plastic flow is not uniform; a boundary layer of reduced plastic flow is found. The same boundary value problem is also solved within the framework of the nonlocal plasticity theory of Fleck and Hutchinson (1993, 1997) and Shu and Fleck (1999). The nonlocal theory also gives rise to a boundary layer for particular choices of higher-order boundary conditions. The predictions of the two theories are compared for a range of strip thicknesses with the aim of ascertaining the predicted size dependence that emerges from each framework. Additional physical insight is gained via simple crack models for representing single slip and symmetric double slip. These models capture several of the overall features of the slip distribution within the strip, including the shape of the average stress versus average strain response of the strip, but are unable to predict the details of the boundary layer.

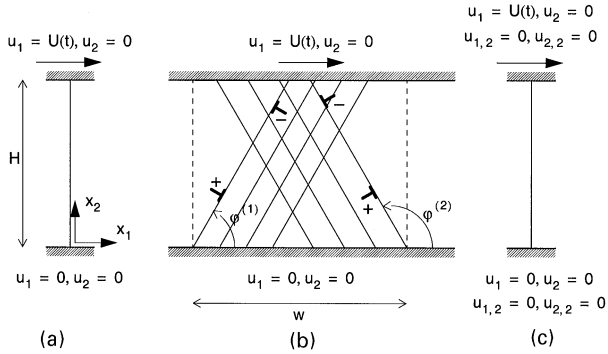

Fig. 1. Illustration of the problem formulation and boundary conditions for simple shear of an elastic–plastic layer of thickness H assuming (a) standard local continuum plasticity; (b) discrete dislocation plasticity with two active slip systems; (c) gradient plasticity.

2. Problem formulation

The calculations are carried out within the context of a small displacement gradient formulation, and Cartesian tensor notation is used throughout. Simple shear of a crystalline strip, of height H in the x_2-direction, is considered, with shearing along the x_1-direction, see Fig. 1. Plane strain and quasi-static loading conditions are assumed, and the strip is unbounded in the x_1- and x_3-directions. Several constitutive descriptions of the strip are used, each of which gives rise to a different boundary value problem.

For a classical continuum constitutive relation, the boundary value problem can be expressed in terms of the principle of virtual work,

$$\int_V \sigma_{ij}\delta\varepsilon_{ij}\,\mathrm{d}V = \int_S T_i\delta u_i\,\mathrm{d}S, \tag{1}$$

where $\delta(\ )$ denotes a variation, u_i are the displacement components, σ_{ij} is the stress tensor and

$$\varepsilon_{ij} = \frac{1}{2}(u_{i,j} + u_{j,i}), \quad T_i = \sigma_{ij}n_j \tag{2}$$

with n_i the normal to S and $(\ )_{,i}$ denoting differentiation with respect to x_i. The boundary conditions are (see Fig. 1a)

$$u_1 = 0, \quad u_2 = 0 \quad \text{along } x_2 = 0,$$

$$u_1 = U(t) = H\dot{\Gamma}t, \quad u_2 = 0 \quad \text{along } x_2 = H, \tag{3}$$

where $\dot{\Gamma}$ is the prescribed shear rate, t is time and $(\dot{\ })$ denotes $\partial(\ )/\partial t$. The solution to this simple shearing boundary value problem is independent of x_1 and equilibrium requires σ_{12}, the only non-vanishing stress component for an isotropic solid, to be spatially uniform. If the material properties are homogeneous this implies that the only non-vanishing strain component, ε_{12}, is also spatially uniform. Thus, the deformation

state is one of homogeneous shearing with

$$u_1 = \dot{\Gamma} t x_2 = \Gamma x_2, \quad \varepsilon_{12} = \varepsilon_{21} = \frac{1}{2}\Gamma, \quad \omega_{12} = -\omega_{21} = \frac{1}{2}\Gamma, \tag{4}$$

where $\omega_{ij} = (u_{i,j} - u_{j,i})/2$ denotes the rotation tensor. All other strain and rotation components vanish.

When the material is characterized as an elastic–plastic solid with plastic flow arising from the collective motion of discrete dislocations, the boundary value problem is still governed by Eqs. (1)–(3). However, the response will not in general be independent of x_1. In this case, we require all field quantities to be periodic in x_1 with period w (see Fig. 1b); for example, $u_i(x_1, x_2) = u_i(x_1 + kw, x_2)$ for any integer k. The homogeneous solution for the classical solid obviously also satisfies this periodicity condition. What is important for the following is that the discrete dislocations are blocked when they reach the edges $x_2 = 0$ or H.

We also consider nonlocal theories of plasticity involving higher-order stresses that are work conjugates to the strain gradients entering the formulation. The principle of virtual work now takes the form

$$\int_V [\sigma_{ij}\delta\varepsilon_{ij} + \tau_{ijk}\delta\eta_{ijk}]\,\mathrm{d}V = \int_S [T_i\delta u_i + r_i\delta u_{i,n}]\,\mathrm{d}S, \tag{5}$$

where $u_{i,n}$ is the normal derivative of the displacement at the surface S, $\tau_{ijk} = \tau_{jik}$ is called the double stress and

$$\eta_{ijk} = \varepsilon_{ij,k}. \tag{6}$$

As for the conventional continuum, all field quantities are independent of x_1. As a consequence, ε_{11} equals zero and the only non-vanishing strain components are $\varepsilon_{12} = \varepsilon_{21} = \gamma(x_2)/2$ and ε_{22}. From Eq. (6), the non-vanishing strain-gradient components are $\eta_{122} = \eta_{212}$ and η_{222}. The non-vanishing in-plane stress components are σ_{11}, $\sigma_{12} = \sigma_{21}$ and σ_{22} and the non-vanishing double stress components are τ_{112}, $\tau_{212} = \tau_{122}$, τ_{222}, τ_{111}, $\tau_{121} = \tau_{211}$ and τ_{221}. The traction and higher-order traction components that enter the external virtual work expression in Eq. (5) on $x_2 = 0$ and H are given by

$$T_1 = \sigma_{12} - \tau_{122,2}, \quad T_2 = \sigma_{22} - \tau_{222,2} \tag{7}$$

and

$$r_1 = \tau_{122}, \quad r_2 = \tau_{222}. \tag{8}$$

In addition to the boundary conditions (3), either r_1 or $u_{1,2}$ and either r_2 or $u_{2,2}$ must be prescribed. If $r_1 = r_2 = 0$ is prescribed on $x_2 = 0$ and H, it follows that the solution for the nonlocal theory is spatially homogeneous, all gradients vanish identically and there is no difference between the predictions of corresponding local and nonlocal theories. On the other hand, if the higher-order boundary conditions are taken to be that the normal displacement derivatives vanish (see Fig. 1c), i.e.

$$u_{1,2} = 0, \quad u_{2,2} = 0 \quad \text{along } x_2 = 0, H \tag{9}$$

then the nonlocal theory can give rise to a non-homogeneous deformation state, as will be seen subsequently.

The appropriate choice of higher-order boundary condition in higher-order theories is a matter of choice, guided by the underlying physics of the boundary. For example, at a fixed boundary plastic straining may be constrained, but the geometric boundary condition that emerges from virtual work (5) is that the total displacement gradient be prescribed, which includes both elastic and plastic contributions. At a stress-free boundary, the traction of course vanishes. However, a vanishing traction does not necessarily imply a vanishing higher-order traction (in a beam, a vanishing shear force does not imply vanishing moment and vice versa).

The predictions of the discrete dislocation theory and nonlocal theory will be presented in terms of the average shear stress τ_{ave} within the strip and its work-conjugate, the applied strain Γ, where

$$\tau_{\text{ave}} = \frac{1}{V}\int_V \sigma_{12}\,\mathrm{d}V = \frac{1}{w}\int_0^w T_1(x_1, x_2)\,\mathrm{d}x_1. \tag{10}$$

2.1. Nonlocal plasticity

Fleck and Hutchinson (1997) and Shu and Fleck (1999) have presented crystal versions of strain-gradient plasticity. The strain ε_{ij} and the strain gradient η_{ijk} are each decomposed into the sum of elastic and plastic parts, with a superscript 'e' denoting the elastic part, and a superscript 'p' denoting the plastic part. Although η_{ijk} is the spatial gradient of ε_{ij}, in general η^{e}_{ijk} differs from the spatial gradient of $\varepsilon^{\text{e}}_{ij}$ and η^{p}_{ijk} differs from the spatial gradient of $\varepsilon^{\text{p}}_{ij}$.

Each slip system is defined by its unit vector along the slip direction $s_i^{(\alpha)}$ and a conjugate unit vector $m_i^{(\alpha)}$ normal to the slip plane. We confine attention to planar crystals having either a single slip system oriented at an angle $\phi^{(1)}=\phi$ from the x_1-axis or having two symmetrically oriented slip systems with $\phi^{(1)}=\phi$ and $\phi^{(2)}=\pi-\phi$, as sketched in Fig. 1b. A Greek superscript, ranging from 1 to 2, denotes a slip system.

The plastic strain rate is related to the slip rate $\dot{\gamma}^{(\alpha)}$ via

$$\dot{\varepsilon}^{\text{p}}_{ij} = \sum_{\alpha} \dot{\gamma}^{(\alpha)}\mu_{ij}^{(\alpha)}, \tag{11}$$

where the Schmid orientation tensor $\mu_{ij}^{(\alpha)}$ is given by

$$\mu_{ij}^{(\alpha)} = \frac{1}{2}[s_i^{(\alpha)}m_j^{(\alpha)} + s_j^{(\alpha)}m_i^{(\alpha)}]. \tag{12}$$

Similarly, the plastic part of the strain gradient (6) has a rate $\dot{\eta}^{\text{p}}_{ijk}$ given by

$$\dot{\eta}^{\text{p}}_{ijk} = \sum_{\alpha} [\dot{\gamma}_S^{(\alpha)}\Psi_{Sijk}^{(\alpha)} + \dot{\gamma}_M^{(\alpha)}\Psi_{Mijk}^{(\alpha)}], \tag{13}$$

where

$$\Psi_{Sijk}^{(\alpha)} \equiv \mu_{ij}^{(\alpha)}s_k^{(\alpha)}, \quad \Psi_{Mijk}^{(\alpha)} \equiv \mu_{ij}^{(\alpha)}m_k^{(\alpha)} \tag{14}$$

are third-order orientation tensors. The quantities $\dot{\gamma}_S^{(\alpha)}$ and $\dot{\gamma}_M^{(\alpha)}$ are the so-called 'micro-slip rate gradients' along the slip direction $s_i^{(\alpha)}$ and the slip normal $m_i^{(\alpha)}$, respectively.

They are independent kinematic quantities and are not tied to the spatial gradient of the slip rate $\dot{\gamma}^{(\alpha)}$.

The plastic work rate per unit volume is written as

$$\dot{W}^{\mathrm{p}} = \sigma_{ij}\dot{\varepsilon}^{\mathrm{p}}_{ij} + \tau_{ijk}\dot{\eta}^{\mathrm{p}}_{ijk} = \sum_{\alpha} [\tau^{(\alpha)}\dot{\gamma}^{(\alpha)} + Q^{(\alpha)}_{S}\dot{\gamma}^{(\alpha)}_{S} + Q^{(\alpha)}_{M}\dot{\gamma}^{(\alpha)}_{M}] \tag{15}$$

and substitution of Eqs. (11) and (13) into Eq. (15) provides an explicit expression for the work conjugate Schmid stress $\tau^{(\alpha)}$ and resolved double stresses $(Q^{(\alpha)}_{S}, Q^{(\alpha)}_{M})$ as,

$$\tau^{(\alpha)} = \sigma_{ij}\mu^{(\alpha)}_{ij}, \quad Q^{(\alpha)}_{S} = \tau_{ijk}\Psi^{(\alpha)}_{Sijk}, \quad Q^{(\alpha)}_{M} = \tau_{ijk}\Psi^{(\alpha)}_{Mijk}. \tag{16}$$

It is mathematically convenient to assume that yield of a given slip system (α) occurs when an overall scalar effective stress $s^{(\alpha)}$ attains a yield value $s^{(\alpha)}_{\mathrm{y}}$. The effective stress $s^{(\alpha)}$ is taken to depend on the resolved stress-like quantities $(\tau^{(\alpha)}, Q^{(\alpha)}_{S}, Q^{(\alpha)}_{M})$ in the following quadratic manner:

$$(s^{(\alpha)})^2 = (\tau^{(\alpha)})^2 + (\ell_S^{-1}Q^{(\alpha)}_{S})^2 + (\ell_M^{-1}Q^{(\alpha)}_{M})^2, \tag{17}$$

where the length scales (ℓ_S, ℓ_M) have been introduced for dimensional consistency and are internal material length scales of the constitutive description.

The slip rate $\dot{\gamma}^{(\alpha)}$ and microslip rate gradients $(\dot{\gamma}^{(\alpha)}_{S}, \dot{\gamma}^{(\alpha)}_{M})$ are assumed to obey the normality rule

$$\dot{\gamma}^{(\alpha)} = \dot{\gamma}^{(\alpha)}_{\mathrm{e}}\frac{\tau^{(\alpha)}}{s^{(\alpha)}}, \quad \dot{\gamma}^{(\alpha)}_{S} = \ell_S^{-2}\dot{\gamma}^{(\alpha)}_{\mathrm{e}}\frac{Q^{(\alpha)}_{S}}{s^{(\alpha)}}, \quad \dot{\gamma}^{(\alpha)}_{M} = \ell_M^{-2}\dot{\gamma}^{(\alpha)}_{\mathrm{e}}\frac{Q^{(\alpha)}_{M}}{s^{(\alpha)}}, \tag{18}$$

where the effective strain rate $\dot{\gamma}^{(\alpha)}_{\mathrm{e}}$ is obtained by substituting Eq. (18) into Eq. (17), giving

$$\dot{\gamma}^{(\alpha)}_{\mathrm{e}} = [(\dot{\gamma}^{(\alpha)})^2 + \ell_S^2(\dot{\gamma}^{(\alpha)}_{S})^2 + \ell_M^2(\dot{\gamma}^{(\alpha)}_{M})^2]^{1/2}. \tag{19}$$

Since only slip gradients in the slip plane are related to the storage of geometrically necessary dislocations, we use $\ell_M \to \infty$ in the calculations here (Shu and Fleck, 1999).

It remains to stipulate a hardening relation for the yield strength $s^{(\alpha)}_{\mathrm{y}}$ of each slip system (α) in terms of $\gamma^{(\alpha)}_{\mathrm{e}}$. In the present study we consider the case of single slip, and the case of symmetric double slip, with identical values of $s^{(\alpha)}_{\mathrm{y}}$ and $\gamma^{(\alpha)}_{\mathrm{e}}$ on both slip systems. Consequently, we can write the hardening relation in incremental form as

$$\dot{s}^{(\alpha)}_{\mathrm{y}} = h_{\mathrm{c}}(s^{(\alpha)}_{\mathrm{y}})\dot{\gamma}^{(\alpha)}_{\mathrm{e}}, \tag{20}$$

where h_{c} is the hardening modulus for each slip system at a stress level $s^{(\alpha)}_{\mathrm{y}}$.

The constitutive description is completed by writing

$$\dot{\sigma}_{ij} = L_{ijkl}\dot{\varepsilon}^{\mathrm{e}}_{ij}, \quad \dot{\tau}_{ijm} = \ell_{\mathrm{e}}^2 L_{ijkl}\dot{\eta}^{\mathrm{e}}_{klm} \tag{21}$$

with the isotropic elastic moduli specified by

$$L_{ijkl} = \frac{E}{1+\nu}\left[\frac{1}{2}(\delta_{ik}\delta_{jl} + \delta_{il}\delta_{jk}) + \frac{\nu}{1-2\nu}\delta_{ij}\delta_{kl}\right], \tag{22}$$

where E is Young's modulus, ν is Poisson's ratio and ℓ_{e} is the elastic characteristic length. For the case of symmetric double slip, a direct correspondence exists between

the crystal theory formulation and the simpler, isotropic hardening elastic–plastic strain gradient theory of Fleck and Hutchinson (1997), as shown in Appendix A.

A finite element method is used to determine the deformation history. From Eqs. (21) and (11) through (20), tangent moduli and higher-order tangent moduli are obtained for use in the principle of virtual work (5). Since all field quantities are functions of x_2 only, the governing rate equations are discretized by expanding the displacement fields $u_1(x_2)$ and $u_2(x_2)$ in terms of Hermite cubic polynomials that have the required C_1-continuity. Integration within each element is performed using second-order Gauss–Legendre quadrature. Time integration is carried out in a linear incremental manner with an equilibrium correction used to maintain equilibrium as deformation proceeds. The numerical procedure simplifies considerably for symmetric double slip. In that special case, the only non-vanishing strain and strain gradient components are $\varepsilon_{12} = \varepsilon_{21}$ and $\eta_{122} = \eta_{212}$, and the non-vanishing stress and double stress components are $\sigma_{12} = \sigma_{21}$ and $\tau_{122} = \tau_{212}$, respectively. The correspondence between the crystal plasticity theory and the phenomenological theory was exploited to simplify the calculations for symmetric double slip.

2.2. Discrete dislocation framework

In a discrete dislocation plasticity description, dislocations are represented as line defects in a linear elastic continuum (see e.g. Nabarro, 1967; Hirth and Lothe, 1968). Consistent with the continuum plasticity description, elasticity is assumed to be isotropic and governed by the moduli (22). The method of solution for boundary value problems of the type considered here is that in Van der Giessen and Needleman (1995) and Cleveringa et al. (1999), and is briefly outlined below.

The computation of the deformation history is carried out in an incremental manner. Each time step Δt involves three main computational stages: (i) determining the forces on the dislocations, i.e. the Peach–Koehler force; (ii) determining the rate of change of the dislocation structure, which involves the motion of dislocations, the generation of new dislocations and their mutual annihilation; and (iii) determining the stress and strain state for the current dislocation arrangement.

Here, attention is confined to two-dimensional problems with straight edge dislocations (each having Burgers vector magnitude b) on multiple, possibly intersecting slip planes. The fields for a single dislocation in an infinite medium can be found in standard texts, such as Nabarro (1967) and Hirth and Lothe (1968). Since we are performing a periodic cell analysis, for every dislocation inside the cell $0 \leq x_1 < w$ (Fig. 1) there are replicas in all the other cells. Because of the long-range fields, summing over these replicas numerically may lead to artificial organization of dislocations (Gulluoglu et al., 1989). Similar to Van der Giessen and Needleman (1995), we therefore perform the summation over all replicas analytically, as outlined in Appendix B. Assuming dislocation glide only, the variation of the potential energy of the body due to infinitesimal variations of the position of the kth dislocation is governed by the Peach–Koehler force $f^{(k)}$ given by

$$f^{(k)} = n_i^{(k)} \sigma_{ij} b_j^{(k)}, \tag{23}$$

with $n_i^{(k)}$ the slip plane normal and the Burgers vector $b_j^{(k)}$ of dislocation k. The direction of this force is in the slip plane and normal to the dislocation line.

The magnitude of the glide velocity $v^{(k)}$ of dislocation k is taken to be linearly related to the Peach–Koehler force through the drag relation

$$f^{(k)} = Bv^{(k)}, \tag{24}$$

where B is the drag coefficient. Annihilation of two dislocations with opposite Burgers vector occurs when they are within a material-dependent, critical annihilation distance $L_e = 6b$.

New dislocations are generated by simulating Frank–Read sources. In two dimensions, a Frank–Read source is simulated by point sources on the slip plane which generate a dislocation dipole when the magnitude of the Peach–Koehler force at the source exceeds the critical value $\tau_{nuc}b$ during a period of time t_{nuc}. The distance L_{nuc} between the dislocations is specified as

$$L_{nuc} = \frac{G}{2\pi(1-\nu)}\frac{b}{\tau_{nuc}}, \tag{25}$$

with $2G = E/(1+\nu)$, where G is the shear modulus. At this distance, the shear stress of one dislocation acting on the other is balanced by the slip plane shear stress. The magnitude of τ_{nuc} is randomly chosen from a Gaussian distribution with mean strength $\bar{\tau}_{nuc}$. An initial distribution of dislocation sources is specified on each slip plane.

The two-dimensional edge dislocation model neglects line tension effects and significantly restricts the type of dislocation interactions that can occur. On the other hand, the only constitutive rules needed are Eq. (24) for the dislocation velocity, the annihilation distance, L_e, and Eq. (25) for dislocation nucleation; all other aspects of the formulation follow directly from elasticity theory.

The displacement and stress fields are written as the superposition of two fields

$$u_i = \tilde{u}_i + \hat{u}_i, \quad \sigma_{ij} = \tilde{\sigma}_{ij} + \hat{\sigma}_{ij}. \tag{26}$$

The ($\tilde{}$) displacement field is the superposition of the fields of the individual dislocations (inside the cell, along with all its replicas) in an infinite medium of the homogeneous matrix material and the ($\hat{}$) fields represent the image fields that correct for the actual boundary conditions. The ($\hat{}$) fields are smooth and are solved for by the finite element method. Both the stress–strain response and the evolution of the dislocation structure are outcomes of the boundary value solution in the discrete dislocation formulation.

3. Discrete dislocation predictions

We report results of simulations for a crystal with two slip systems, oriented at $\phi^{(1)} = 60^\circ$ and $\phi^{(2)} = 120^\circ$ with respect to the x_1-direction of shear. The crystal properties are essentially identical to those used in previous studies (Cleveringa et al., 1999, 2000). Isotropic elastic properties are assumed with shear modulus $G = 26.3$ GPa and Poisson's ratio $\nu = 0.33$, the magnitude of the Burgers vector is $b = 0.25$ nm and the dislocation drag coefficient in Eq. (24) is taken to be $B = 10^{-4}$ Pa s, all of which are

representative for aluminum (Kubin et al., 1992). Initially the material is assumed to be dislocation free, and in most computations, sources are randomly distributed over the slip planes. In cases with random sources, their strength is assumed to have a Gaussian distribution with mean value $\bar{\tau}_{\text{nuc}} = 1.9 \times 10^{-3} G$ and standard deviation $0.2\,\bar{\tau}_{\text{nuc}}$ (this corresponds to a mean nucleation distance of $L_{\text{nuc}} = 125b$). The nucleation time for all sources is taken as $t_{\text{nuc}} = 2.6 \times 10^{6} B/G$.

In all cases, the width of the periodic cell (Fig. 1b) is taken to be $w = 1$ μm and we vary the height H of the strip between 0.5 and 3 μm. Also, $\dot{U}$ in Eq. (3) is adjusted so that the overall shear rate $\dot{\Gamma}$ is always $0.38 \times 10^{-11} G/B = 10^{3}$ s^{-1}. In addition to b and H, there are two other material length scales, namely the spacing between active slip planes, d, and the linear spacing of sources on each slip plane, d_{nuc}. The latter corresponds to an area density $\rho_{\text{nuc}} = 1/(d_{\text{nuc}} d)$. The source density, ρ_{nuc} or d_{nuc}, will be assumed to be constant for each computation, although there is no direct physical reason for this density not to evolve during the process. The discrete dislocation results will thus depend on three nondimensional lengths: for example, d/b, H/d, d_{nuc}/d.

The finite element mesh used to solve the problem for the ($\hat{}$) fields in Eq. (26) uses square bilinear elements. The element size is $\lambda = w/30$, irrespective of the height of the strip. Cleveringa et al. (1999) have demonstrated that for meshes of this size there is no significant mesh-size dependence and this has been verified for the present problem. In order to make a connection with the continuum predictions, where quantities are dependent only on x_2, we can average field quantities along the x_1-direction. Making use of the periodicity of the solution over the cell $x_1 \in (0, w)$, we will define the average horizontal displacement, $u_1^{\text{ave}}(x_2)$, and use this to define the shear strain across the strip

$$\gamma(x_2) = \frac{\mathrm{d}u_1^{\text{ave}}}{\mathrm{d}x_2}, \quad u_1^{\text{ave}}(x_2) = \frac{1}{w}\int_0^w u_1(x_1, x_2)\,\mathrm{d}x_1. \tag{27}$$

The value of γ is typically computed at points between the nodes in the x_2-direction.

3.1. Single slip

We start out by considering some simple cases of a strip of height $H = 1$ μm in which only slip system 1 is activated ($\phi^{(1)} = 60^{\circ}$). We assume 1 active slip plane within the cell ($d = 0.87$ μm, giving $H/d = 1.15$), and 2 active slip planes within the cell ($d = 0.43$ μm, giving $H/d = 2.3$); in both cases, a single source is located at the center of the slip plane with $\tau_{\text{nuc}} = \bar{\tau}_{\text{nuc}} = 1.9 \times 10^{-3} G$. In addition, we consider a much finer spacing of slip planes $d = 0.0125$ μm ($H/d = 80$), and with two random sources per plane ($d_{\text{nuc}}/d = 46$) of mean strength $\bar{\tau}_{\text{nuc}}$. Fig. 2 shows the distribution of $\gamma(x_2)$ according to Eq. (27) for two of the cases at various levels of overall shear strain Γ. The strain profiles exhibit serrations that are due to the discrete dislocation distributions, examples of which are shown in Fig. 3. Yet, more importantly, even in some smooth sense, γ is not constant across the strip thickness but exhibits smaller values near the edges $x_2 = 0$ and $x_2 = H$ of the strip.

The origin of the boundary layers obviously lies in the distribution of dislocations. Fig. 3a shows that the dislocations at a given overall strain Γ are organized in rather long pile-ups against the edges when the slip plane spacing is rather large ($H/d = 2.3$).

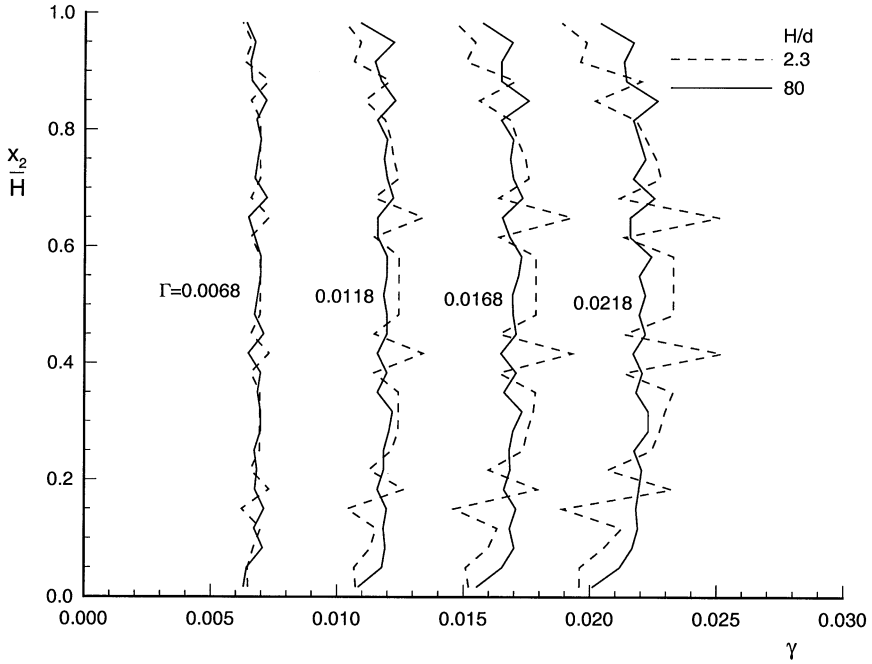

Fig. 2. Shear strain profiles at various values of the overall shear strain Γ for two cases with single slip at $\phi^{(1)} = 60^\circ$.

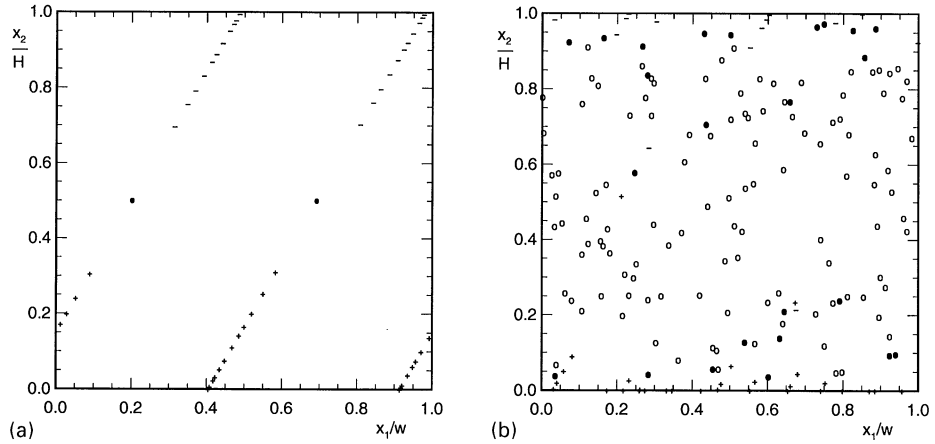

Fig. 3. Dislocation distributions in the unit cell at $\Gamma = 0.0168$ for the two cases shown in Fig. 2: (a) $H/d = 2.3$, (b) $H/d = 80$. Positive and negative dislocations are shown by "+" and "−" symbols, respectively. Open symbols "o" denote the sources, while activated sources are shown by the corresponding filled symbols.

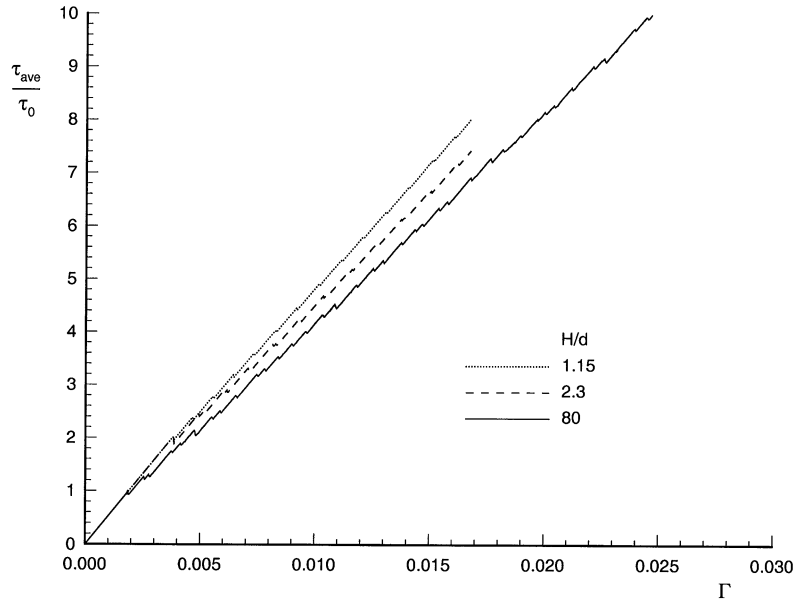

Fig. 4. Average shear stress response to applied macroscopic shear Γ for three single slip cases with various slip plane spacings H/d. The hardening is due to back stresses caused by the dislocation pile-ups seen in Fig. 3.

When there are many more slip planes available, Fig. 3b for $H/d = 80$, the dislocations are more evenly distributed in the x_1-direction, with much shorter pile-ups against the edges. In fact, the distribution in the latter case can be idealized as a horizontal string of relatively close-spaced positive dislocations along $x_2 = 0$ and one of opposite sign along $x_2 = H$. The slip distributions resulting from these two dislocations distributions are obviously different, giving rise to the different strain profiles of Fig. 2.

Both dislocation distributions give rise to long-range stresses in the sheared crystals, which serve as a back stress against the overall shear stress τ_{ave}. As a consequence, the overall stress–strain response shown in Fig. 4 exhibits enormous hardening after yield (the reference stress τ_0 in Fig. 4 is the mean source strength τ_{nuc}). Note that the initial yield point for $H/d = 80$ is significantly lower since the strength of the sources is random in this case.

3.2. Double slip

The results change dramatically when both slip systems are active. The stress–strain response for the above case ($H = 1$ μm) for relatively close-spaced slip planes ($H/d = 80$) but now with double slip is shown in Fig. 5. After a relatively sharp yield peak, the stress response, on average, increases almost linearly with strain, but with a much smaller average tangent modulus than in Fig. 4. This suggests a much smaller back stress than in single slip. Again, the hardening is attributed to the fact that the inclined

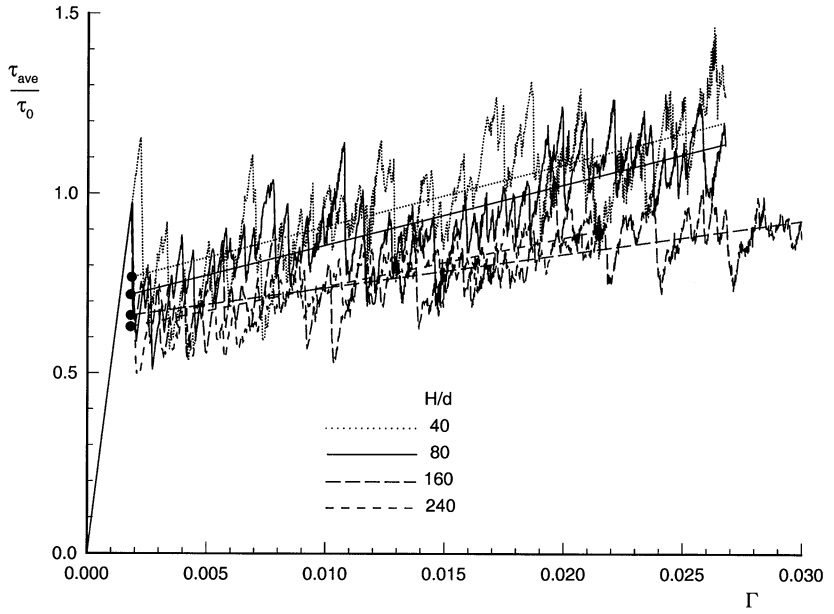

Fig. 5. Average shear stress response to applied macroscopic shear Γ during double slip for various layer thicknesses H/d. In all cases, the slip plane spacing is equal to $d = 50b$ and the linear source spacing is $d_{\text{nuc}} = 0.577\ \mu\text{m} = 46d$.

slip planes are blocked by the top and bottom of the strip; if one of the slip planes would have been parallel to the x_1-direction, slip would have been unhindered, resulting in a nearly perfectly plastic (or even slightly softening) response (see Cleveringa et al., 1997). The pronounced serrations in the plastic regime are due to the many discrete events of dislocation generation and annihilation (which take place in all the unit cells simultaneously).

The strain profiles across the crystal, shown in Fig. 6, are also significantly different from the single slip results (Fig. 2). In fact, the boundary layer in double slip is more pronounced, with the local shear strain $\gamma(x_2)$ approaching values close to zero at both edges $x_2 = 0$ and H. An exponential relation has been fitted to each of the γ profiles in order to facilitate identification of the boundary layer width. Fig. 6 then suggests that the boundary layer width increases significantly with ongoing strain, but this is somewhat exaggerated by this way of presentation; if all profiles are normalized with the corresponding average strain Γ, the widening is still present but less pronounced. Also note that the fluctuations in $\gamma(x_2)$ amplify as the applied strain increases, thus giving rise to the development of rather unsymmetric profiles at the largest Γ shown.

The differences between double and single slip are further substantiated by the dislocation structures that develop. Fig. 7 shows the dislocation distribution for the double slip case considered above at the same overall strain ($\Gamma = 0.0168$) as for the single slip case in Fig. 3b. Even though the slip plane spacing and the linear source spacing are the same ($H/d = 80$, $d_{\text{nuc}}/d = 46$), the two dislocation distributions are noticeably

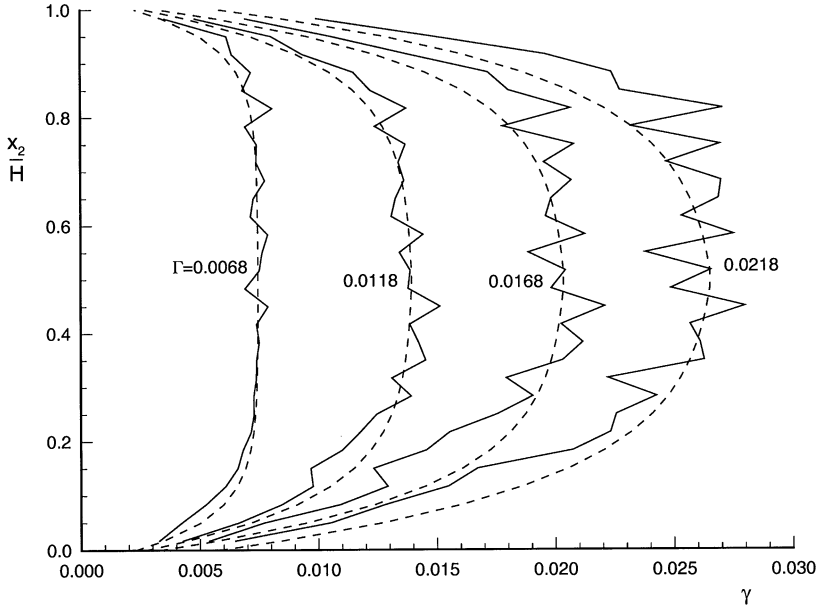

Fig. 6. Shear strain profiles at various values of the applied shear Γ for the case with double slip with $H = 1$ μm shown in Fig. 5. The dashed lines are fitted exponential strain profiles.

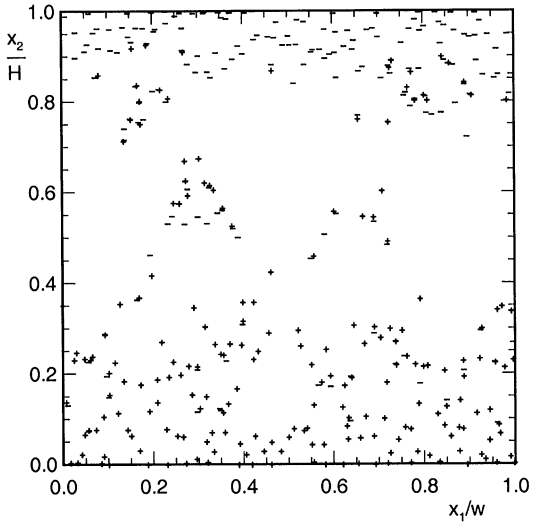

Fig. 7. Dislocation distribution in the unit cell at $\Gamma = 0.0168$ for the double-slip case of Fig. 6.

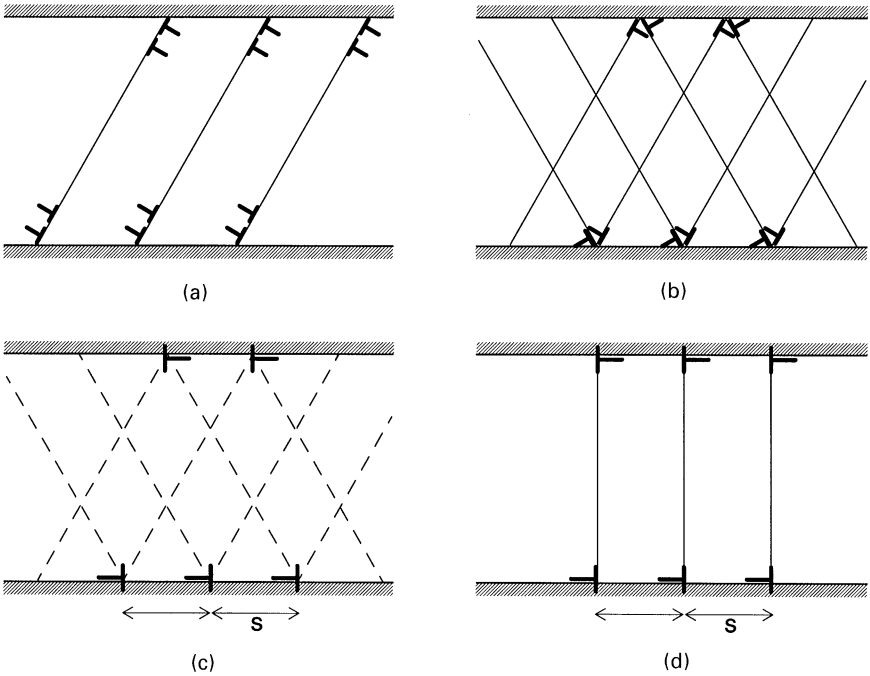

Fig. 8. Schematics of the dislocation distributions in (a) single and (b) double slip. In the latter, couples of dislocations near the edges react to form "super" dislocations with Burgers vector in the x_2-direction (c), which suggests the mode II crack model (d) discussed in Section 5.1.

different in three respects: (i) the overall dislocation density is much higher in double slip, with (ii) a layer of like-signed dislocations near the edges and (iii) a significant density in the core of the crystal. The higher density of mobile dislocations is consistent with the much lower hardening rate. The absence of a strong back stress in double slip allows dislocation sources throughout the crystal to be activated, rather than just the small fraction activated in single slip (Fig. 3b). Many of the dislocations generated in double slip move towards the edges and form a layer of rather densely packed dislocations, with a thickness of roughly $0.2H$ which is roughly the same as the width of the boundary layer in the strain profile of Fig. 6. Nevertheless, a significant fraction of the dislocations move in the central core of the crystal, leading to the very inhomogeneous shear strain distribution shown in Fig. 6.

Thus, the key to the noted differences lies in the presence of back stresses in single slip and in their absence in double slip: the back stresses that would develop due to piling-up on one of the slip systems (Fig. 8a) are easily relaxed by the generation of dislocations on the other slip system. In double slip, the resolved shear stress on both slip systems is the same, and this leads to the concentration of like-signed dislocations at each of the edges (Fig. 8b). The Burgers vectors of both families of dislocations, $\pm bs_i^{(1)}$ and $\pm bs_i^{(2)}$, combine to give dislocations with a Burgers vector in the x_2-direction, as illustrated in Fig. 8c. Thus, the densely packed layers of disloca-

tions near the crystal edges can be idealized as two "walls" of dislocations of opposite sign with some spacing s at a distance H. These "super" dislocations would be termed "geometrically necessary dislocations" in Ashby's (1970) terminology. The configuration in Fig. 8c is well-known (Nabarro, 1967) to produce bending of the crystal in between the walls, leading to displacements u_1, the gradient of which, $\mathrm{d}u_1/\mathrm{d}x_2$, is qualitatively consistent with the strain profiles shown in Fig. 6. Also, the long-range stress fields of individual dislocations are partially canceled in such dislocation walls, so that the stress caused by a dislocation wall is significant only over a distance of the order of the spacing s. This explains why back stresses are negligible in double slip compared to those in single slip which are due, in contrast, to the long-range stress fields of dislocation pile-ups.

The idealized picture in Fig. 8 can be confronted with the more complex simulation results by extracting from the latter the average density ρ_i of the net Burgers vector in the x_i-direction. Making use of periodicity, this quantity is computed as the x_i-component of the net Burgers vector over the width w of the cell in a strip of height λ (the element size) at position x_2, i.e.

$$\rho_i(x_2) = \frac{1}{w\lambda} \sum_k b_i^{(k)}, \quad \forall k \text{ such that } x_2 - \lambda/2 < x_2^{(k)} < x_2 + \lambda/2. \tag{28}$$

For the ideal dislocation distribution of Fig. 8c, ρ_1 vanishes identically while $\rho_2(x_2)$ has peaks at $x_2 = 0$ and H. The results for the single versus the double slip simulations for $H/d = 80$ at $\Gamma = 0.0168$ are shown in Fig. 9. For single slip, ρ_1 and ρ_2 have a fixed ratio independent of x_2 and both exhibit local peaks near the edges and are basically zero everywhere else; this is consistent with the dislocation distribution shown in Fig. 3b. For double slip, ρ_1 and ρ_2 are uncoupled; ρ_1 vanishes throughout the crystal, while $\rho_2(x_2)$ has very distinct peaks near the edges, which indicates that the dislocations indeed organize in effectively walls of dislocations with net Burgers vector in the x_2-direction, albeit that the walls have a certain width. In fact, the $\rho_2(x_2)$-distribution has a width that is again roughly equal to the width of the boundary layer in the strain profile in Fig. 6. This demonstrates that the boundary layer in the shear strain distribution in double slip is directly related to the density of the geometrically necessary dislocations with net Burgers vector along x_2.

Continuing with the idealized picture of two opposite walls forming along the edges with continued macroscopic straining, it is to be expected that the boundary layer widths in $\gamma(x_2)$ as well as in $\rho_2(x_2)$ are controlled by the spacing of the super dislocations in the wall (Fig. 8c). This spacing is bounded from below by the potential slip plane spacing d. However, not all potential slip planes are active while those that are active are not equally active. This is clearly observed in the deformed finite element mesh shown in Fig. 10 corresponding to the dislocation distribution in Fig. 7. Even though the mesh cannot exhibit all the fine slip bands that are actually formed, it does show that slip tends to concentrate in a number of bands parallel to each of the two slip systems. From this picture, the average spacing between such slip bands at this value of Γ is roughly $10d$ (or $H/10$).

Finally, we return to the stress–strain curves for double slip shown in Fig. 5. In this figure, the response is also shown for crystal strips that are narrower ($H = 0.5$ μm)

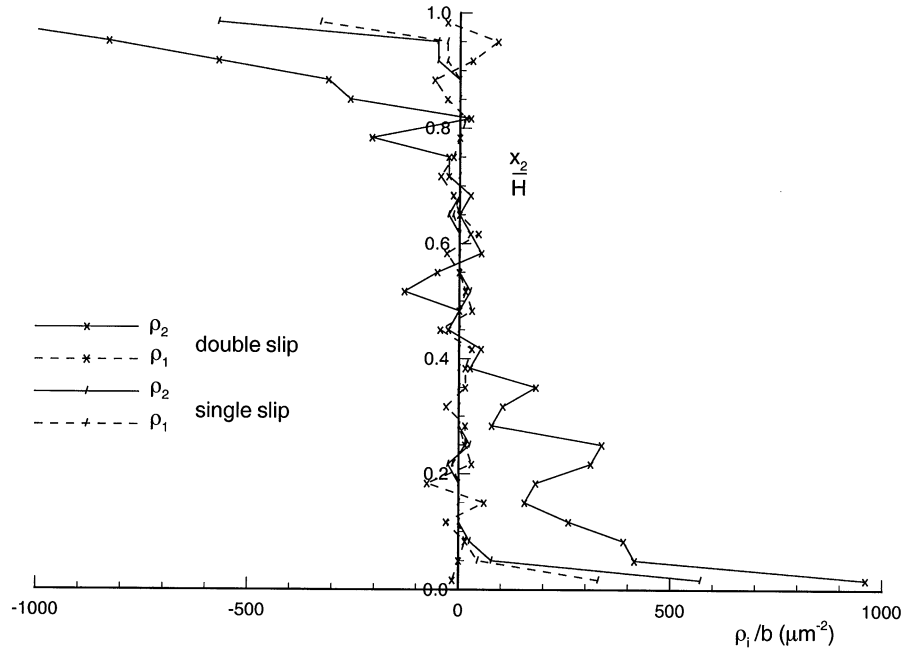

Fig. 9. The net dislocation density distributions according to Eq. (28) corresponding to the dislocation distributions for single slip of Fig. 3b and for double slip of Fig. 7.

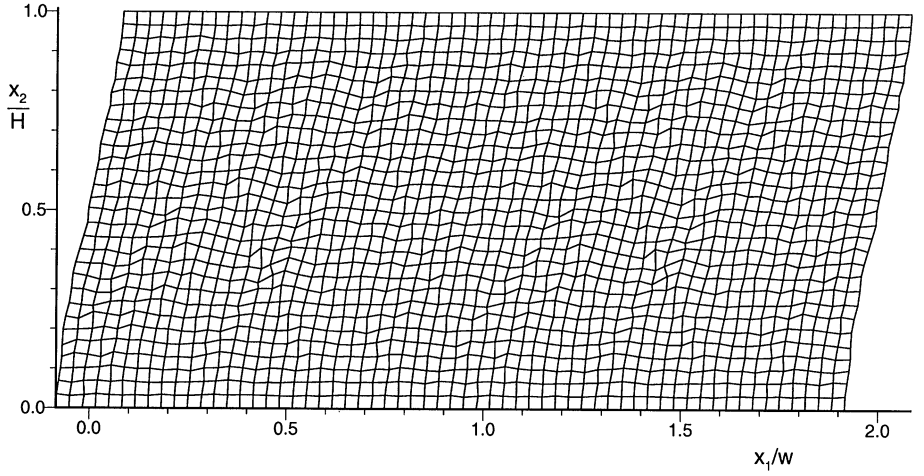

Fig. 10. Deformed mesh of two unit cells for the double-slip case of Figs. 6 and 7 at $\Gamma = 0.0168$. The displacements are amplified by a factor of 10 for clarity.

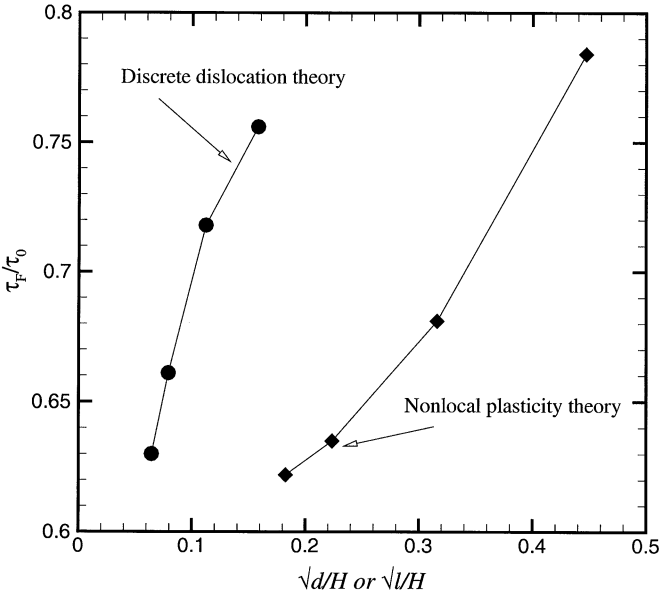

Fig. 11. The back-extrapolated flow stress τ_F versus the relative layer height H/d according to the discrete dislocation calculations, for the cases shown in Fig. 5 (marked by the dots). Also shown is the double slip nonlocal theory prediction for τ_F versus the relative layer thickness H/ℓ, with $\ell_e = \ell$.

or wider ($H = 2$ or 3 μm) than the one considered so far. The material properties, in particular the slip plane spacing d and the source spacing d_{nuc}, are the same. Each of the hardening responses is seen to be linear on average and is fitted by a straight line. The dots indicate the initial back-extrapolated flow stresses, τ_F. We observe that the tangent modulus reduces gradually as the crystal height becomes smaller, although the values for the largest crystals do not order. The initial flow stresses, however, do exhibit a clear size effect, with the smallest crystal having the highest yield strength. In fact, Fig. 11 shows that these values of τ_F scale almost linearly with $\sqrt{d/H}$, as one would expect for the Hall–Petch effect (e.g., Petch, 1953; Armstrong et al., 1962; Hansen, 1985; Rao et al., 1995).

4. Nonlocal theory predictions

In this section, the predictions of the nonlocal crystal theory are summarized for both symmetric double slip and single slip. In order to make direct comparisons with the predictions of discrete dislocation theory, the underlying hardening behavior of the nonlocal theory was chosen to give the same average shear stress τ_{ave} versus shear strain Γ response in symmetric double slip as the discrete dislocation model, for a strip thickness of $H = 3$ μm. This was achieved by assuming a shear yield strength $s_y^{(1)} = 0.3085\tau_0$ and a constant hardening modulus $h_c = 7.22\tau_0$ with τ_0 again equal to the mean nucleation strength in the discrete dislocation calculations. Consequently, the

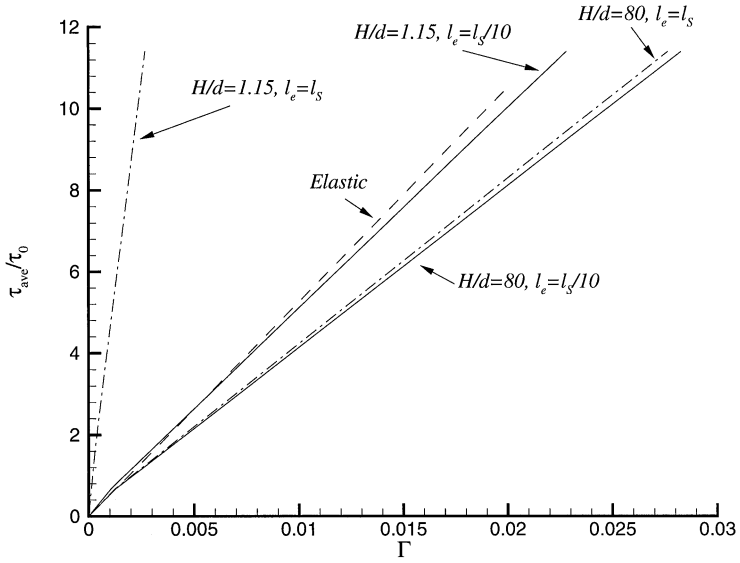

Fig. 12. Shear traction τ_{ave} versus average shear strain Γ predicted by single-slip nonlocal theory, with selected values of layer thickness H/d and elastic length scale ℓ_{e}. In all cases, $\ell_S = d$.

τ_{ave} versus Γ curve has a tangent modulus of $G_{\text{T}} = 14\tau_0$ compared to an initial shear modulus $G = 526\tau_0$.

4.1. Single slip

First, consider the predictions of the nonlocal theory for single slip ($\phi^{(1)} = 60^\circ$). As mentioned previously, we take $\ell_M \to \infty$, and unless otherwise stated, the higher-order boundary conditions (9) are enforced. Numerical experimentation revealed that the shear strain distribution across the strip thickness gives a reasonable fit to the discrete dislocation distribution with $\ell_S = 10\ell_{\text{e}} = d$, where d is the spacing of slip planes. Calculations of the average shear stress τ_{ave} versus shear strain Γ in the strip, with $\ell_S = d$, are shown in Fig. 12 for the choices $\ell_S = 10\ell_{\text{e}}$ and $\ell_S = \ell_{\text{e}}$, for both $H/d = 1.15$ and 80. In addition, the elastic response has been plotted for the case of uniform shear. We note that the elastic–plastic calculation with $\ell_S = \ell_{\text{e}}$ and $H/d = 1.15$ leads to a stiffer response than the homogeneous elastic case. This is why the elastic length scale is taken to be $\ell_{\text{e}} = \ell_S/10$. The τ_{ave} versus Γ response becomes much less sensitive to the assumed value of ℓ_{e} for large values of H/d, such as the case $H/d = 80$, as shown in Fig. 12.

The shear strain distribution within the strip is plotted in Fig. 13 for the cases $H/d = 2.3$ and 80 with $\ell_S = 10\ell_{\text{e}} = d$ for various levels of average strain Γ. Enforcement of the higher-order boundary conditions (9) results in a vanishing shear strain $\gamma = 0$ on the boundaries and gives rise to the presence of boundary layers. The boundary layer thicknesses are quite different fractions of the strip height but are about $0.6d$ for

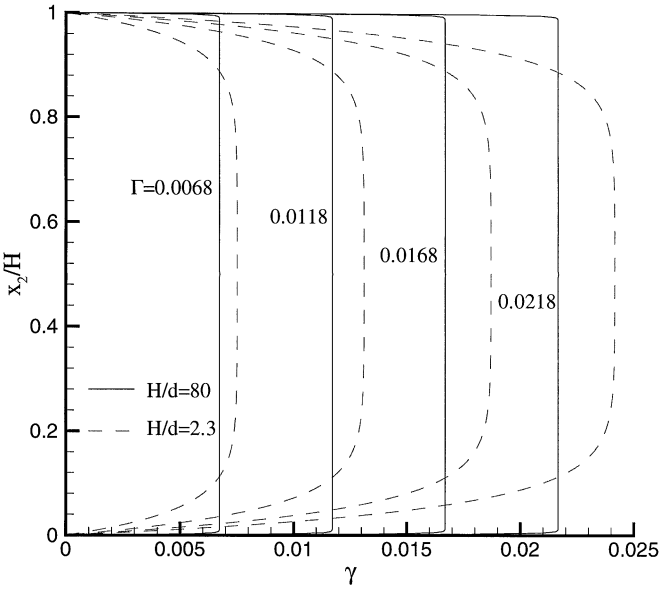

Fig. 13. Shear strain profiles at various values of the overall shear strain Γ predicted by single-slip nonlocal theory, at selected levels of average shear strain Γ, and $H/d = 2.3$ and 80.

both $H/d = 2.3$ and 80; this thickness is relatively insensitive to the overall level of strain Γ.

The effect of the choice of higher-order boundary condition upon the single slip response is now explored for the case $H/d = 2.3$ and $\ell_S = 10\ell_e = d$. Specifically, the τ_{ave} versus Γ response and the shear strain across the strip are plotted in Figs. 14 and 15, respectively, for a number of assumed higher-order boundary conditions associated with zero work along the boundary. On taking these two figures together, we note that a stiffer response and a pronounced boundary layer are displayed by taking $u_{1,2} = u_{2,2} = 0$ or $u_{1,2} = r_2 = 0$ on the boundaries; a somewhat more compliant response is associated with $r_1 = u_{2,2} = 0$ or $r_1 = r_2 = 0$, in which case the shear strain remains uniform across the strip. We conclude that a switch in boundary condition from $u_{2,2} = 0$ to $r_2 = 0$ plays only a minor role; this is not surprising by the following argument: continuity of displacement on the boundary dictates that $u_{1,1} = 0$, and for an incompressible solid we have directly $u_{2,2} = 0$. Although plastic straining is incompressible, elastic straining involves a small volume change and so $u_{2,2}$ is small but not zero.

4.2. Double slip

Second, consider the predictions for symmetric double slip ($\phi^{(1)} = 60^\circ$, $\phi^{(2)} = 120^\circ$) by the nonlocal theory. The same magnitude of size effect for the discrete dislocation and nonlocal theories is achieved in the symmetric double slip case by adopting a plastic length scale $\ell = \ell_S/\sin\phi^{(1)} = 0.1$ μm, where ℓ is defined in Eq. (A.9), and

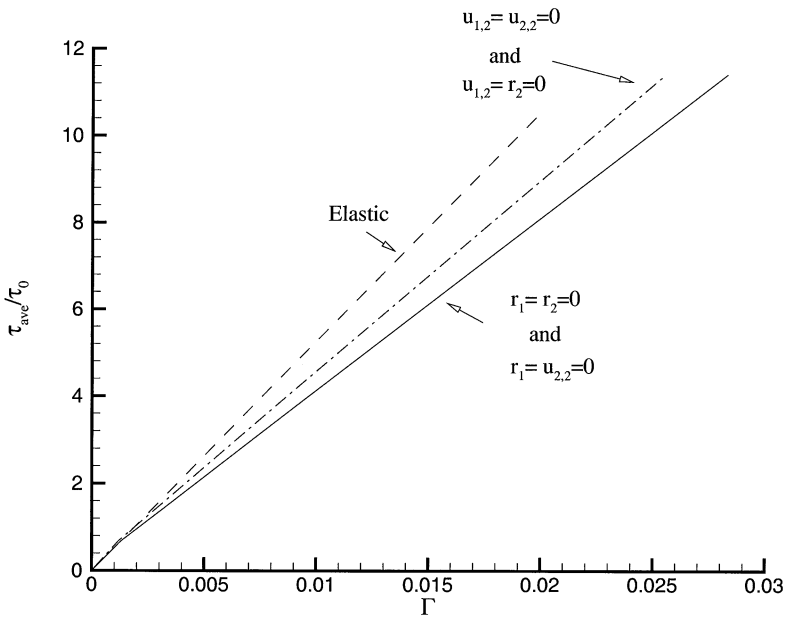

Fig. 14. Effect of choice of boundary conditions upon the shear traction τ_{ave} versus average shear strain Γ response by single-slip nonlocal theory, for $H/d = 2.3$ and $\ell_S = 10\ell_e = d$.

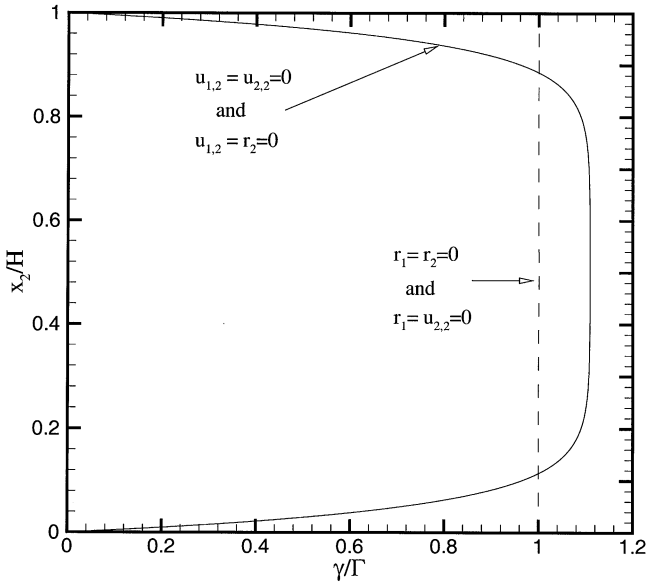

Fig. 15. Effect of choice of boundary conditions upon the shear strain profile by single-slip nonlocal theory, at an overall shear strain $\Gamma = 0.0218$. $H/d = 2.3$ and $\ell_S = 10\ell_e = d$.

$\ell_e = \ell$, as follows. The average shear stress τ_{ave} versus average shear strain Γ response is plotted in Fig. 16 for $H/\ell = 5$–30, corresponding to four values of strip thickness H in the range 0.5–3 μm. When H/ℓ is reduced from 30 to 5, the back-extrapolated yield strength τ_F increases by a factor of about 30% for the case $\ell_e = \ell$ as shown in Fig. 16a, but remains constant for the choice $\ell_e = 0.1\ell$ used above for single slip, as shown in Fig. 16b. Results shown in the previous section for the discrete dislocation theory give an increase in strength of about 30% when H is reduced from 3 to 0.5 μm, and this motivates the choice $\ell_e = \ell = 0.1$ μm for symmetric double slip.

The constrained shear problem addressed in this study is a prototype of the plastic constraint which exists at the grain boundaries of a polycrystal, due to the anisotropy of plastic slip between neighboring grains. It is instructive to include in Fig. 11 the back-extrapolated yield strength τ_F against $\sqrt{\ell/H}$ as predicted by the nonlocal theory. We observe that τ_F scales approximately with $\sqrt{\ell/H}$, although the plot shows a somewhat upward curvature. In contrast, the discrete dislocation predictions display a small downward curvature, see Fig. 11. Recall that the discrete dislocation results shown in Fig. 11 are for the choice $d = 0.0125$ μm. The value $\ell = 0.1$ μm was adopted for the nonlocal theory in order for its predictions to match those of the discrete dislocation calculations: though not shown explicitly, the two curves of Fig. 11 overlap closely upon taking $\ell = 8d$.

The shear strain distribution across the strip γ, normalized by the average value Γ, is given in Fig. 17 for the case $H = 1$ μm ($H/\ell = 10$), at four selected values of average strain Γ in the range 0.0068 to 0.0218 (the discrete dislocation result is shown in Fig. 6). At all strain levels, γ drops to zero at the boundaries of the strip, as demanded by the higher-order boundary condition of the nonlocal theory. The shear strain distribution is approximately parabolic in shape, and the shape of the distribution is almost insensitive to the strain level Γ. It is difficult to define a precise thickness of the boundary layer adjacent to the rigid substrates. At any rate, it appears that the value of H/ℓ is sufficiently small for any boundary layer to exist across the full thickness of the strip. In order to investigate this further, the distribution of γ/Γ across the thickness of the strip is plotted in Fig. 18 against H for selected values of H/ℓ over the range 5–30, and with Γ held fixed at 0.0218. A well-defined boundary layer of thickness about 7ℓ is evident for the cases $H/\ell = 20$ and 30. The boundary layer stretches across the full thickness of the strip for smaller values of H/ℓ, as already noted.

5. Simple models

As is well known, cracks in planar elastic solids are mathematically equivalent to certain continuous distributions of dislocations along the crack faces. Conversely, the dislocation distributions in Section 3, especially the schematic ones in Fig. 8a and d, can be idealized in terms of an array of parallel mode II cracks. An array of traction-free cracks subject to simple shear has been analyzed by Fleck (1991) using the method of distributed dislocations. In general such cracks are mixed mode, having both an opening (mode I) and a sliding (mode II) response to the imposed loading. When the cracks are constrained so that only the mode II response is permitted, then the response

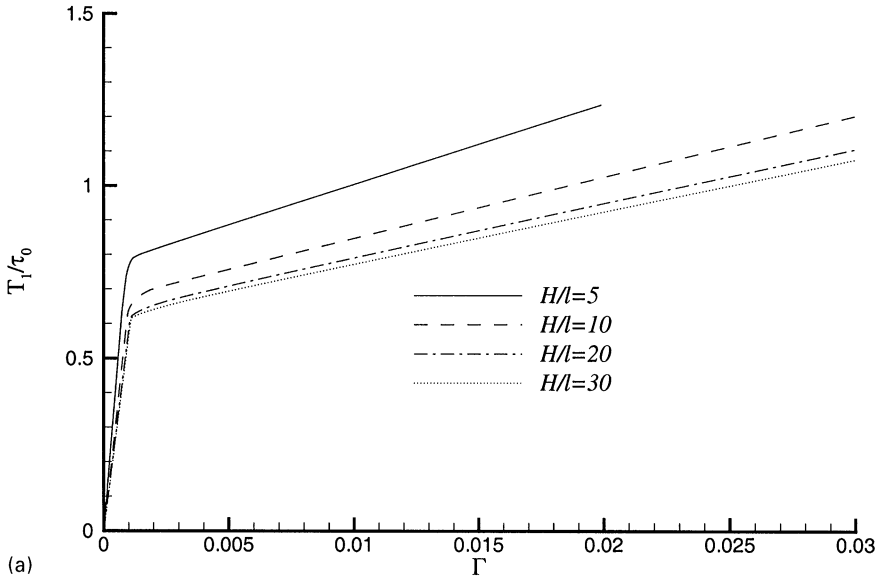

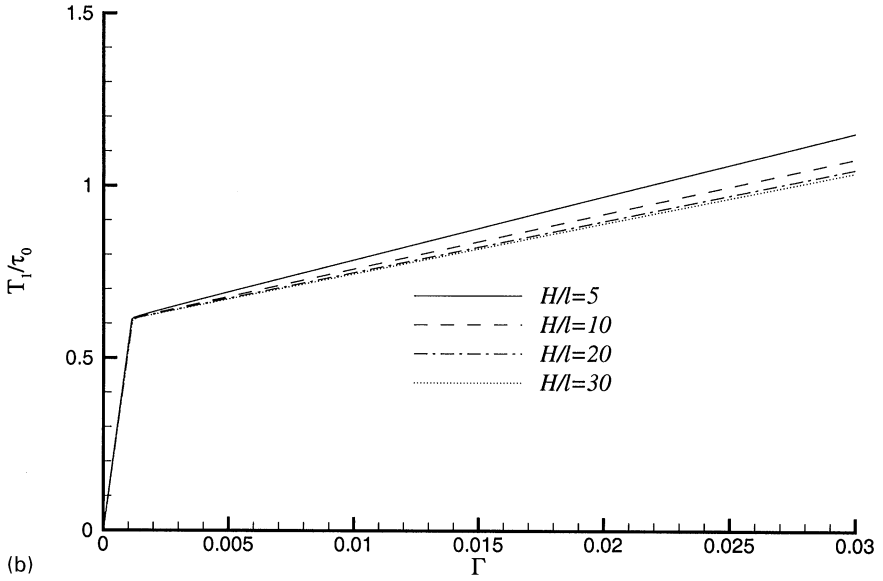

Fig. 16. Shear traction τ_{ave} versus average shear strain Γ predicted by nonlocal theory for symmetric double slip, for selected values of layer thickness H: (a) $\ell = \ell_e$, (b) $\ell = 10\ell_e$.

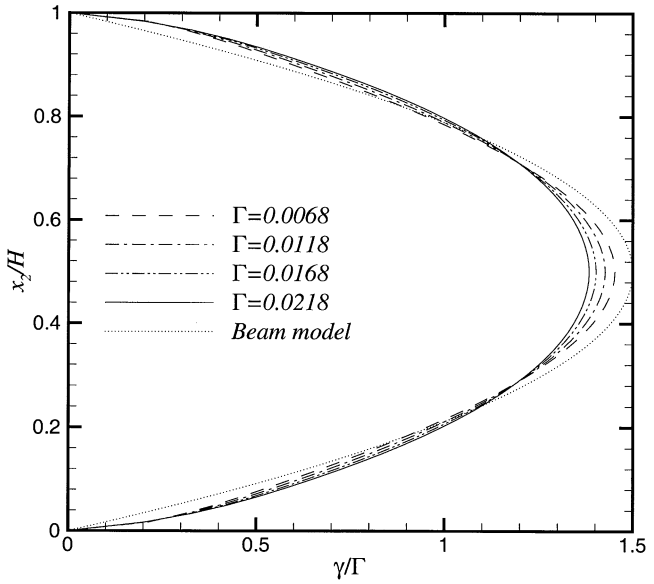

Fig. 17. Shear strain profiles at various values of the overall shear strain Γ predicted by the nonlocal theory for symmetric double slip, with $H/\ell = 10$ and $\ell = \ell_e$. The predictions of the beam model (34) are included, by taking the limit $s/H \to 0$.

of an array of inclined slip bands in an infinite elastic solid is obtained. We assume that the change in stiffness due to the presence of the slip bands is the same for a solid which is finite in the x_2-direction as it is for the infinite solid. For single slip, the orientation of the cracks corresponds to the orientation of the slip system (Fig. 8a), while for symmetric double slip, the cracks are parallel to the x_2-axis (Fig. 8d).

Here, attention is focused on two limiting cases: (i) for symmetric double slip, the ligament between neighboring cracks can be modeled as a beam and (ii) for closely spaced inclined slip bands, the ligament between the bands is homogeneously deforming.

5.1. Crack model for symmetric double slip

Consider an array of parallel, frictionless model II cracks of length H in an infinite elastic solid subject to a remote shear stress τ_∞. The cracks are parallel to the x_2-axis, with spacing s along the x_1-axis, and plane strain conditions prevail. The numerical procedure of Fleck (1991) has been used to obtain the compliance of the cracked strip as a function of crack spacing. The numerical results for the strip compliance over the full range $0 \le H/s \le \infty$ are adequately fitted (to within 0.3%) by the expression

$$\frac{U}{H\tau_\infty} = \frac{1}{G} + \frac{(1-\nu^2)}{E}\frac{H}{s}\left(\frac{\pi}{2} + \frac{H}{s}\right)\left(1 - 0.195\sin\frac{\pi H}{H+s}\right), \tag{29}$$

where U is the total displacement jump across the cracked strip, corresponding to an average strain $\Gamma = U/H$ in the strip.

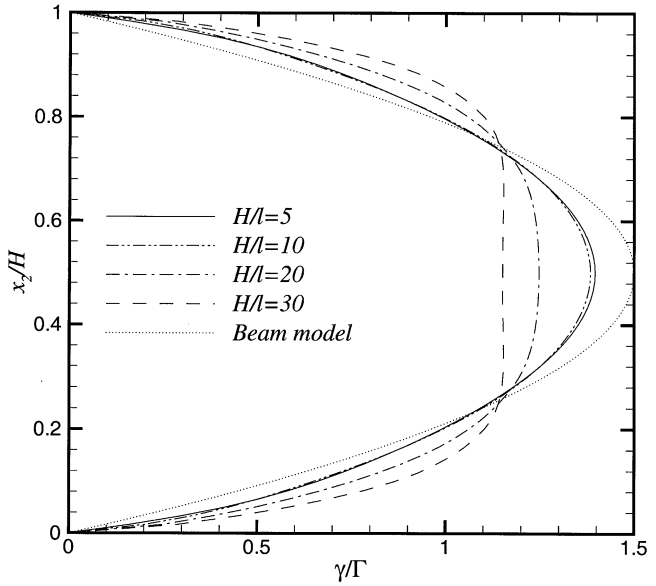

Fig. 18. Shear strain profiles for selected values of layer thickness H at an overall shear strain $\Gamma = 0.0218$, as predicted by the nonlocal theory for symmetric double slip, with $\ell = \ell_e$. The predictions of the beam model (34) are included, by taking the limit $s/H \to 0$.

In the present study, the slip planes are assumed to be sufficiently closely spaced for the beam theory limit ($H/s \gg 1$) to apply, and analytical expressions can then be obtained for the displacement field within the cracked strip. Accordingly, the additional displacement due to the presence of the cracks is calculated by treating the ligaments between cracks as beams in bending. The shear force $s\tau_\infty$ on each beam gives rise to a bending moment $s\tau_\infty(x_2 - \frac{1}{2}H)$. Consequently, the additional transverse displacement along the beam mid-plane is given by

$$\Delta u_1(x_2) = 3(1-\nu^2)\frac{\tau_\infty}{E}\frac{H^3}{s^2}\left[\left(\frac{x_2}{H}\right)^2 - \frac{2}{3}\left(\frac{x_2}{H}\right)^3\right]. \tag{30}$$

On recalling that the displacement jump across the strip in the absence of the crack array is $H\tau_\infty/G$, we express the total displacement jump across the strip, U, by

$$U = \frac{H\tau_\infty}{G} + \frac{(1-\nu^2)\tau_\infty}{E}\frac{H^3}{s^2}. \tag{31}$$

This expression is in agreement with Eq. (29) in the limit $H/s \gg 1$. The effective shear modulus for the cracked strip, $G_{\text{eff}} \equiv H\tau_\infty/U$, follows immediately as

$$\frac{1}{G_{\text{eff}}} = \frac{1}{G} + \frac{(1-\nu^2)}{E}\left(\frac{H}{s}\right)^2. \tag{32}$$

The crack model may also be used to estimate the distribution of shear strain and the dislocation density across the strip. The shear strain $\gamma(x_2) = \partial u_1/\partial x_2$ follows

from Eq. (30) as

$$\gamma = \frac{\tau_\infty}{G} + \frac{6(1-\nu^2)\tau_\infty}{E}\left(\frac{H}{s}\right)^2\left[\left(\frac{x_2}{H}\right) - \left(\frac{x_2}{H}\right)^2\right] \tag{33}$$

and, after normalizing by the average strain in the strip Γ, can be stated as

$$\frac{\gamma}{\Gamma} = \frac{1 + 3(1-\nu)(H/s)^2\,(1 - x_2/H)\,x_2/H}{1 + \frac{1}{2}(1-\nu)\,(H/s)^2}. \tag{34}$$

The mode II sliding displacement across each crack is $(\gamma - (\tau_\infty/G))s$ and the density of net Burgers vector ρ_2 along the cracks is the gradient of this sliding displacement so that

$$\rho_2 = -\frac{\partial \gamma}{\partial x_2} = \frac{12(1-\nu^2)\tau_\infty}{s^2 E}x_2. \tag{35}$$

Shen et al. (1998) have developed a similar mode II crack model to explain the dependence on film thickness of the linear hardening behavior of a thin copper film deposited onto a silica substrate.

5.2. Crack model for single slip

We now consider a single set of closely spaced parallel shear cracks in a strip of height H inclined at angle ϕ from the x_1-axis. The strip is fixed at $x_2 = 0$ and the additional displacements at $x_2 = H$ are $(\Delta u_1, \Delta u_2)$. Each ligament between neighboring cracks is considered to be homogeneously deformed. It is convenient to introduce a coordinate system where one direction is parallel to the cracks and the other direction is orthogonal to the plane of each crack. These will be termed the longitudinal (L) and transverse (T) directions, respectively. It is also convenient to introduce the angle β defined by $\beta = \pi/2 - \phi$.

Because the cracks are frictionless, the shear stress vanishes on each crack surface. Hence, the shear stress $\sigma_{LT} = 0$ in each ligament. As a consequence, equilibrium requires

$$\sigma_{LL} = \sigma_{22} + \sigma_{12}\tan\beta, \quad \sigma_{TT} = \sigma_{22} - \frac{\sigma_{12}}{\tan\beta}, \tag{36}$$

where σ_{22} and σ_{12} are the normal stress and shear stress, respectively.

Under the imposed shear, the displacement jump across the ligament is related to the change in inclination, $\Delta\phi$, by

$$\Delta u_T = \frac{H}{\sin\phi}\Delta\phi \tag{37}$$

while the transverse strain, ε_{TT}, and longitudinal strain, ε_{LL}, are given by

$$\varepsilon_{TT} = \Delta\phi\tan\beta, \quad \varepsilon_{LL} = \frac{\Delta u_L}{H}\sin\phi, \tag{38}$$

where Δu_L is determined from the condition that $\Delta u_2 = 0$ giving

$$\Delta u_2 = \Delta u_L\cos\beta + \Delta u_T\sin\beta = 0. \tag{39}$$

The strain state in the ligament is known from Eqs. (37)–(39). Then, using the plane strain, isotropic stress–strain relations, we find

$$\sigma_{TT} = -\sigma_{LL} = \frac{E}{(1+\nu)}\Delta\phi \tan\beta. \tag{40}$$

The additional shear displacement in the ligament, $\Delta u_1 = \Delta u_L \sin\beta - \Delta u_T \cos\beta$, simplifies from Eqs. (37)–(39) to

$$\Delta u_1 = -\frac{H\Delta\phi}{\cos^2\beta}. \tag{41}$$

Equilibrium (36) finally gives $\sigma_{12} = G_{\text{eff}}\Delta u_1/H$ where the effective shear modulus G_{eff} is

$$G_{\text{eff}}/G = \sin^2 2\beta = \sin^2 2\phi. \tag{42}$$

5.3. Predictions

Consider first the predictions of the crack model for single slip. The relation (42) suggests that the tangent stiffness G_{eff} after yield is 0.75 times the initial elastic value G for a slip plane inclination of $\phi^{(1)} = 60^\circ$. The nonlocal theory supports this for sufficiently thick strips; for example, in Fig. 12 the tangent modulus beyond yield equals $0.755G$ for the case $H/d = 80$ ($\ell_e = \ell_S = d$). Also the discrete dislocation calculations reveal that for the same large strip thickness the post-yield tangent modulus is 0.75 times the initial modulus, see Fig. 4. The tangent modulus increases with diminishing H due to the increasing dominance of the boundary layer, according to both the nonlocal and the discrete dislocation theories. The simple crack model for single slip neglects any boundary layer effects and predicts a uniform shear strain throughout the strip. A more sophisticated crack model, as developed by Fleck (1991) using the method of distributed dislocations, could be used to predict reduced shear strains at the boundaries of the cracked strip; in essence, the more sophisticated version would include the effects of beam bending in the vicinity of the boundaries. Such additional sophistication to the crack model is not warranted, as it lacks much of the physics of the discrete dislocation theory, particularly near the boundaries of the elastic–plastic strip. The simple crack model for single slip suggests that the density of geometrically necessary dislocations vanishes throughout the strip. The discrete dislocation calculations support this, with the proviso that near the boundaries, where the simple crack model is inappropriate, the dislocation density becomes large, as shown in Fig. 9.

Next, we compare the predictions of the crack model for symmetric double slip with those for the nonlocal and discrete dislocation theories. First, we note that in order to bring the tangent modulus according to Eq. (32) in line with the low post-yield tangent modulus predicted by discrete dislocation plasticity as shown in Fig. 5, we have to choose a beam thickness to height ratio s/H as small as roughly 0.1. Then, for the evaluation of the strain profile from Eq. (34) one can practically take the limit of $s/H \to 0$. This results in a parabolic profile, which has been included in Fig. 18 for comparison with the strain profiles of the nonlocal theory at $\Gamma = 0.0218$ and H/ℓ in the range 5–30. It is seen that the simple crack model predicts a strain profile which varies

across the full width of the strip, and not a boundary layer adjacent to each interface. Consequently, the crack model is in approximate agreement with the predictions of the nonlocal theory in the regime where the boundary layer straddles the full height of the strip ($H/\ell \leq 10$). At larger values of H/ℓ the predictions of the two models diverge, and the nonlocal theory suggests that the boundary layer is of width about 6ℓ, with a uniform shear strain near the mid-plane of the strip.

The predictions of the simple crack model for symmetric double slip are also included in Fig. 17; this shows the shear strain profile for $H/\ell = 10$ and four levels of average strain Γ. According to the nonlocal theory, the strain profile flattens slightly with increasing Γ so that the parabolic profile as given by the crack model becomes increasingly inaccurate at higher strain levels.

The crack model for symmetric double slip suggests a linear distribution ρ_2 of geometrically necessary dislocations across the strip, (35). Although it is difficult to make precise statements about the shape of the dislocation distribution from the discrete dislocation calculations, due to fluctuations that arise from the discreteness of the distribution, Fig. 9 does suggest that the density ρ_2 varies linearly with depth for double slip, except for enhanced values adjacent to the boundaries. Again, the simple crack model provides insight into the nature of the dislocation distribution, but fails to describe the deformation state within the boundary layer.

6. Discussion

For a classical elastic–plastic solid, the solution to the boundary value problem analyzed is a state of homogeneous simple shear. When plastic flow is modeled in terms of the collective motion of discrete dislocations, the response is far more complex. Even in an average sense the deformation is not uniform across the strip, and the average strain distribution depends sensitively on the geometry of slip. Furthermore, there is a distinct size effect, with smaller being harder.

The non-uniformity of the average deformation and the size effect arise from slip being blocked at the upper and lower boundaries of the strip. The gradient of shear strain across the strip implies the presence of "geometrically necessary dislocations" in the sense of Ashby (1970). It should be noted however that the term "geometrically necessary" is somewhat misleading, since in this case there is not an imposed strain gradient as in the case of bending (Cleveringa et al., 1999), but the strain gradient develops as a consequence of the edge effect of constrained dislocation glide.

In single slip, the dislocation pile-ups against the boundaries of the strip lead to very large back stresses so that the tangent shear modulus is of the same order as the elastic shear modulus G. Consistent with this, unloading calculations (not shown here) exhibit an extremely strong Bauschinger effect. The overall shear stress versus shear strain response in single slip is remarkably insensitive to the model details.

The situation is quite different for double slip. Dislocation nucleation on the conjugate slip system relaxes the back stress. Consistent with this, the tangent shear modulus is of the order of 10 times the initial flow stress τ_F as compared with a significant fraction of the elastic shear modulus for single slip. Also, unloading calculations (again, not

shown here) exhibit a small Bauschinger effect for double slip. In double slip, the boundary layer is much more significant with strains dropping close to zero near the edges of the strip. The boundary layer thickness is significantly greater than for single slip, and it tends to increase slightly with increasing strain. A clear size effect is found for the initial flow strength τ_F that is consistent with a Hall–Petch inverse square root relation (Fig. 11). However, no such ordered dependence of the tangent shear modulus with size (Fig. 5) emerges from the double slip calculations here. Any relation that may exist is masked by statistical effects.

In the discrete dislocation formulation, the hardening and the dislocation structures that emerge are outcomes of the boundary value problem solution. The extent of the deformation boundary layers and the size effect depend on the model parameters. For example, numerical experimentation revealed that the results depend on the dislocation mobility compared to the shearing rate $\dot{\Gamma}$; at sufficiently low mobility, dislocations tend to stay more in the core region of the strip. Also, calculations showed that if a high Peierls barrier to glide is introduced, glide is effectively prevented and no boundary layers are found. The predicted boundary layer width and size effect depend in principle on all material length scales involved, viz. the slip plane spacing and the source density. This dependence has not been explored in full detail here, but the interpretation in terms of the simple crack model for double slip suggests that the boundary layer width scales with the average spacing between the most active slip bands.

The idealized dislocation structures of Fig. 8c and d are akin to those assumed in Mughrabi's (1983) model for dislocation cells that can evolve as a consequence of self-organization at large strains. Such cells are observed, e.g. Hughes and Hansen (1993), and modeled by the nonlocal theory of Ortiz et al. (2000). Here, however, the focus is on boundary effects that can emerge at relatively small strains, as in the experiments of Sun et al. (2000) on pure aluminum bicrystals, which show a piling-up of geometrically necessary dislocations as seen in the discrete dislocation calculations (Fig. 7).

The present calculations were carried out within a two-dimensional, small strain framework. Three-dimensional effects are expected to be of increasing importance as straining progresses, giving rise, for example, to parabolic hardening by forest dislocation interactions not accounted for in the two-dimensional model and, possibly, to the emergence of dislocation cells. In addition, dislocations piled-up against the boundaries can be relaxed in other ways than just by activating slip on other slip planes, such as by expanding along the screw direction.

A challenge for phenomenological continuum theories of plastic flow is to develop a constitutive framework that exhibits the features that emerge in the discrete dislocation calculations. In this paper, the discrete dislocation predictions have been compared with corresponding predictions of the nonlocal plasticity of Fleck and Hutchinson (1997) and Shu and Fleck (1999). In order to match the predictions under single slip, it is necessary to take $\ell_S = 10\ell_e = d = 0.0125$ μm. This gives a clear link between the slip band spacing d and the constitutive plastic length scale ℓ_S. No such simple picture emerges for the case of symmetric double slip. From the point of capturing the size effect, one needs to choose $\ell = \ell_e = 0.1$ μm, which is roughly $10d$ (recall that $\ell_S = \ell \sin\phi^{(1)} = 0.866\ell$). This is consistent with the active slip band spacing found in

the discrete dislocation calculations, while also the crack model for symmetric double slip gives the same tangent modulus as the discrete dislocation calculation with a crack spacing s equal to $10d$. On the other hand, this value of ℓ overestimates the thickness of the boundary layer in shear strain (Fig. 17). Conversely, smaller values of ℓ would give better correspondence in terms of boundary layer width but the size effect in terms of overall yield response, Fig. 16, would not match well. It is noted that the value of $\ell = 0.1$ μm is significantly smaller than the values around 1 μm that were obtained by fitting to experimental results on wire torsion (Fleck et al., 1994) and other experiments (Fleck and Hutchinson, 1997), but these were all on polycrystals and involved substantially larger strains. In this regard, it is worth noting that in isotropic strain gradient plasticity two distinct length scales have been identified, one mainly associated with stretch gradients that is taken to be 0.25–1 μm, the other associated mainly with rotation gradients where a value of about 5 μm is used (Hutchinson, 2000).

The dependence of the value of the elastic length scale ℓ_e used on the slip mode is noteworthy. The relatively large value for symmetric double slip is needed to predict a size effect comparable to what is obtained in the discrete dislocation calculations; taking $\ell_e = \ell/10$ gives a negligible size effect in symmetric double slip. On the other hand, in single slip, agreement with the discrete dislocation results requires ℓ_e of the order of $\ell/10$; for $\ell_e \approx \ell$, the initial elastic response of the strip is too stiff for small strip thicknesses because of elastic-gradient effects.

Although on physical grounds it is expected that strain-gradient strengthening is by the storage of geometrically necessary dislocations, so that $\ell_M \to \infty$, additional single slip calculations were carried out using $\ell_M = \ell_S$ and the results of these calculations do not differ significantly from those presented here. Furthermore, Eq. (A.9) shows that in symmetric double slip the behavior depends only on the composite length ℓ, not on ℓ_S or ℓ_M individually. On the other hand, in Bassani et al. (2001) results were obtained that were very sensitive to whether or not the hardening depended solely on the gradient associated with geometrically necessary dislocations. A precise delineation remains to be given of the circumstances in which it is important, in a phenomenological nonlocal theory, to include only gradients associated with geometrically necessary dislocations.

For both single slip and double slip, the discrete dislocation calculations give rise to boundary layers that thicken somewhat with increasing strain. Neither the nonlocal continuum plasticity theory calculations carried out here nor the simple crack model predict this feature. It remains to be seen whether or not an alternative formulation, as, for example, in Huang et al. (2000) or Gurtin (2000), gives more accurate boundary layer effect predictions.

7. Conclusions

The constrained shear problem addressed in this study is a prototype of the plastic constraint which exists at the grain boundaries of a polycrystal (e.g. Petch, 1953; Armstrong et al., 1962; Hansen, 1985; Sun et al., 2000), the surface of a thin film

with a passivation layer (e.g. Shen et al., 1998) or at the interfaces in a multilayer (e.g. Rao et al., 1995). Quite general features emerge from our analyses of this model problem:

- In the discrete dislocation simulations, the shear stress averaged over the length of the cell is constant across the strip (as required by equilibrium), but the corresponding shear strain is not. Distinct deformation boundary layers can develop.
- The occurrence and extent of the boundary layer in the discrete dislocation calculations depends on the slip mode (single slip versus double slip) and on the material properties (e.g. the Peierls stress).
- When a boundary layer develops, the nonuniform deformation gives rise to geometrically necessary dislocations and, accordingly, to a size-dependent overall stress–strain response. The size effect is mainly seen on the back-extrapolated flow strength, with a square root size-dependence as consistent with experiment.
- The boundary layer and size effects seen in the simple shear discrete dislocation calculations are not captured by conventional continuum plasticity or by a nonlocal plasticity theory that does not involve higher-order boundary conditions, such as that in Acharya and Bassani (2000).
- In formulations involving higher-order boundary conditions (Fleck and Hutchinson, 1993, 1997; Shu and Fleck, 1999; Huang et al., 2000; Gurtin, 2000), boundary layers and size effects can occur with uniform properties. Whether or not they emerge depends on which higher-order boundary conditions are imposed.
- Calculations based on the higher-order stress framework (Fleck and Hutchinson, 1993, 1997; Shu and Fleck, 1999) give the same qualitative dependence on slip mode as the discrete dislocation simulations, but the evolution of the boundary layer width is not well-reproduced. Also, the value of the elastic length scale that needs to be used to obtain the size dependence of the initial flow strength seen in the discrete dislocation results is larger than can be justified physically.
- Simple analytical crack models exhibit the different evolutions of back stress in single and double slip but do not describe the deformation state within the boundary layer.

Acknowledgements

A. Needleman and E. Van der Giessen acknowledge support from the Materials Research Science and Engineering Center on *On Micro- and Nano-Mechanics of Materials* at Brown University (NSF Grant DMR-0079964). The authors are grateful for several insightful discussions with Profs. M.F. Ashby and Y. Bréchet. Significant parts of this work were carried out during the 1999 program on "Solid Mechanics and Materials Science" at the Isaac Newton Institute for Mathematical Sciences, University of Cambridge. We are grateful for the hospitality and intellectual stimulation enjoyed during that period.

Appendix A. Correspondence of the crystal and phenomenological versions of strain-gradient plasticity for symmetric double slip

A.1. Crystal version for symmetric double slip in shear

Consider the case of simple shear of a crystal with two slip systems ($\alpha = 1, 2$) symmetrically disposed to the x_2-direction, as shown in Fig. 1b. Resolution of stress via Eq. (16) gives

$$\tau^{(1)} = \tau^{(2)} = \sigma_{12}\cos 2\phi, \quad Q_S^{(1)} = Q_S^{(2)} = \tau_{122}\cos 2\phi \sin\phi,$$

$$Q_M^{(1)} = -Q_M^{(2)} = \tau_{122}\cos 2\phi\cos\phi. \tag{A.1}$$

By symmetry we note that $\dot{\gamma}^{(2)} = \dot{\gamma}^{(1)}$, $\dot{\gamma}_S^{(2)} = \dot{\gamma}_S^{(1)}$ and $\dot{\gamma}_M^{(2)} = -\dot{\gamma}_M^{(1)}$. The plastic strain rate is

$$\dot{\varepsilon}_{12}^{\mathrm{p}} = \dot{\varepsilon}_{21}^{\mathrm{p}} = \dot{\gamma}^{(1)}\cos 2\phi, \quad \dot{\varepsilon}_{11}^{\mathrm{p}} = \dot{\varepsilon}_{22}^{\mathrm{p}} = 0 \tag{A.2}$$

and the plastic strain gradient rate is

$$\dot{\eta}_{212}^{\mathrm{p}} = \dot{\eta}_{122}^{\mathrm{p}} = [\dot{\gamma}_S^{(1)}\sin\phi + \dot{\gamma}_M^{(1)}\cos\phi]\cos 2\phi \tag{A.3}$$

with all other $\dot{\eta}_{ijk}^{\mathrm{p}} = 0$. The relation (A.3) can be simplified by elimination of $\dot{\gamma}_M^{(1)}$ as follows; we substitute from Eq. (A.1) into Eq. (18), in order to express $\dot{\gamma}_M^{(1)}$ in terms of $\dot{\gamma}_S^{(1)}$, and thereby obtain

$$\dot{\eta}_{122}^{\mathrm{p}} = \dot{\gamma}_S^{(1)}\frac{\cos 2\phi}{\sin\phi}. \tag{A.4}$$

A.2. Coincidence of crystal theory and phenomenological theory

The isotropic hardening phenomenological theory and strain gradient crystal theory can be brought into coincidence for symmetric double slip by a suitable choice of the magnitude of constitutive parameters. For the isotropic hardening theory in simple shear, there is a single non-vanishing stress component $\sigma_{12} = \sigma_{21}$ and a single non-vanishing double stress component $\tau_{122} = \tau_{212}$. The effective stress measure is

$$\tau_{\mathrm{e}} \equiv \sqrt{\sigma_{12}^2 + \ell^{-2}\tau_{122}^2} \tag{A.5}$$

and its work-conjugate, the effective plastic strain rate, is defined by

$$\dot{\gamma}_{\mathrm{e}} = \sqrt{2}\,[(\dot{\varepsilon}_{12}^{\mathrm{p}})^2 + (\ell\dot{\eta}_{122}^{\mathrm{p}})^2]^{1/2}, \tag{A.6}$$

where the length scale ℓ has been introduced on dimensional grounds.

Associated plastic flow is assumed, with the plastic strain rates $(\dot{\varepsilon}_{12}^{\mathrm{p}}, \dot{\eta}_{122}^{\mathrm{p}})$ expressed as

$$2\dot{\varepsilon}_{12}^{\mathrm{p}} = \dot{\gamma}_{\mathrm{e}}\frac{\partial\tau_{\mathrm{e}}}{\partial\sigma_{12}} = \dot{\gamma}_{\mathrm{e}}\frac{\sigma_{12}}{\tau_{\mathrm{e}}} \quad \text{and} \quad 2\dot{\eta}_{122}^{\mathrm{p}} = \dot{\gamma}_{\mathrm{e}}\frac{\partial\tau_{\mathrm{e}}}{\partial\tau_{122}} = \dot{\gamma}_{\mathrm{e}}\frac{\ell^{-2}\tau_{122}}{\tau_{\mathrm{e}}}. \tag{A.7}$$

The plastic strain rate $\dot{\varepsilon}_{12}^{\mathrm{p}} = \dot{\varepsilon}_{21}^{\mathrm{p}}$ and slip-gradient rate $\dot{\eta}_{122}^{\mathrm{p}} = \dot{\eta}_{212}^{\mathrm{p}}$ in the phenomenological theory are related to the corresponding crystal quantities by Eqs. (A.2) and (A.4),

respectively, and the stresses $(\sigma_{12}, \tau_{122})$ are related to the Schmid stresses ($\tau^{(1)}$, $Q_S^{(1)}$, $Q_M^{(1)}$) via Eq. (A.1). Now, the effective shear stress τ_e and the effective shear strain rate $\dot{\gamma}_e$ are defined by Eqs. (A.5) and (A.6), respectively, whereas the effective stress $s_y^{(1)}$ and effective strain rate $\dot{\gamma}_e^{(1)}$ for slip system 1 are defined by Eqs. (17) and (19), respectively.

On substituting Eq. (A.1) into Eq. (17), $s_y^{(1)}$ can be rewritten as

$$s_y^{(1)} = \cos 2\phi[\sigma_{12}^2 + \tau_{122}^2(\ell_S^{-2}\sin^2\phi + \ell_M^{-2}\cos^2\phi)]^{1/2}. \tag{A.8}$$

After making the choice

$$\ell^{-2} = \ell_S^{-2}\sin^2\phi + \ell_M^{-2}\cos^2\phi \tag{A.9}$$

we obtain the connection between τ_e and $s_y^{(1)}$ according to

$$s_y^{(1)} = \tau_e \cos 2\phi. \tag{A.10}$$

For symmetric double slip, the response depends only on the combination of ℓ_S and ℓ_M in Eq. (A.9). However, to keep the connection with geometrically necessary dislocations, we regard ℓ_M as infinite and $\ell = \ell_S/\sin\phi$ in interpreting the results.

With the hardening rate given by $\dot{\tau}_e = h\dot{\gamma}_e$ in the phenomenological theory, and given by $\dot{s}_y^{(1)} = h_c\dot{\gamma}_e^{(1)}$ in the crystal theory, we obtain the relation

$$h_c = 2h\cos^2 2\phi. \tag{A.11}$$

Identification of the crystal theory to the phenomenological theory is completed by assuming an isotropic elastic response for both theories, as prescribed by Eq. (22).

Appendix B. Fields for periodic dislocation arrangements

Together with all its replicas, any dislocation in the computational cell (Fig. 1) forms an infinitely long string of dislocations with a mutual distance of w. In this appendix we construct the fields for such a string of dislocations in an infinite solid by analytically summing over all dislocations in the string. These fields can then immediately be used for each dislocation as the contribution to the $\tilde{(\ )}$ fields in Eq. (26). [1]

The summation is conveniently done by expressing the fields in terms of Muskhelishvili (1953) functions. With ζ the complex position $\zeta = x_1 + \mathrm{i}x_2$, stress and displacement fields are given then in terms of two analytical functions $\varphi(\zeta)$ and $\psi(\zeta)$ as follows:

$$\frac{1}{2}(\sigma_{22} + \sigma_{11}) = 2\Re\,[\varphi'(\zeta)], \tag{B.1}$$

$$\frac{1}{2}(\sigma_{22} + \sigma_{11}) + \mathrm{i}\sigma_{12} = \bar{\zeta}\varphi''(\zeta) + \psi'(\zeta), \tag{B.2}$$

$$2\mu(u_1 + \mathrm{i}u_2) = (3 - 4\nu)\varphi(\zeta) - \zeta\,\overline{\varphi'(\zeta)} - \overline{\psi(\zeta)}. \tag{B.3}$$

The overbar denotes the complex conjugate, $\Re$ the real part and $\mathrm{i} = \sqrt{-1}$.

[1] The $\tilde{\ }$ is omitted in this appendix for clarity.

For a single dislocation at the origin of ζ in an infinite solid, the functions are given by (Freund, 1994)

$$\varphi'(\zeta) = -\frac{\mu}{4\pi(1-\nu)}\frac{\mathrm{i}b}{\zeta}, \quad \psi'(\zeta) = \frac{\mu}{4\pi(1-\nu)}\frac{\mathrm{i}\bar{b}}{\zeta},$$

where b now is the complex representation of the Burgers vector, $b = b_1 + \mathrm{i}b_2 = |b|(\cos\phi + \mathrm{i}\sin\phi)$ with ϕ the slip plane orientation with respect to the x_1-axis. If the dislocation is at Z, the transformation rules (Muskhelishvili, 1953) imply that the functions read

$$\varphi'(\zeta) = -\frac{\mu}{4\pi(1-\nu)}\frac{\mathrm{i}b}{\zeta - Z}, \quad \psi'(\zeta) = \frac{\mu}{4\pi(1-\nu)}\left[\frac{\mathrm{i}\bar{b}}{\zeta - Z} - \bar{Z}\frac{\mathrm{i}b}{(\zeta - Z)^2}\right]. \tag{B.4}$$

The field for an infinite string of dislocations is now obtained by the summation of the functions φ' and ψ'. We will do this by taking the dislocation in the cell to be at the origin, so that the replicas are positioned at $(x_1, x_2) = (jw, 0)$ or $Z = jw$ $(j = -\infty, \ldots, \infty)$. From Eq. (B.4) we immediately obtain

$$\varphi'(\zeta) = -\sum_{j=-\infty}^{\infty}\frac{\mu}{4\pi(1-\nu)}\frac{\mathrm{i}b}{\zeta - jw} = -\frac{\mu}{4\pi(1-\nu)}\frac{\pi}{w}\mathrm{i}b\cot\left(\pi\frac{\zeta}{w}\right)$$

$$\psi'(\zeta) = \sum_{j=-\infty}^{\infty}\frac{\mu}{4\pi(1-\nu)}\left[\frac{\mathrm{i}\bar{b}}{\zeta - jw} - jw\frac{\mathrm{i}b}{(\zeta - jw)^2}\right]$$

$$= \frac{\mu}{4\pi(1-\nu)}\frac{\pi}{w}\mathrm{i}\left[2\Re(b)\cot\left(\pi\frac{\zeta}{w}\right) - b\left(\pi\frac{\zeta}{w}\right)\csc^2\left(\pi\frac{\zeta}{w}\right)\right].$$

Straightforward differentiation and substitution into Eqs. (B.1) and (B.2) yields the expressions for the stress field of a dislocation and all its replicas.

The calculation of the displacement field requires integration of $\varphi'(\zeta)$ and $\psi'(\zeta)$. Direct integration gives $\varphi(\zeta)$ and $\psi(\zeta)$ as

$$\varphi(\zeta) = \frac{\mu}{4\pi(1-\nu)}\mathrm{i}b\ln\sin\left(\pi\frac{\zeta}{w}\right),$$

$$\psi(\zeta) = -\frac{\mu}{4\pi(1-\nu)}\mathrm{i}\left[\bar{b}\ln\sin\left(\pi\frac{\zeta}{w}\right) + b\left(\pi\frac{\zeta}{w}\right)\cot\left(\pi\frac{\zeta}{w}\right)\right]$$

up to an integration constant. The integration constant has to be chosen carefully in order that the displacement discontinuity (resulting from the multi-valued logarithm in the above expressions for $\varphi(\zeta)$ and $\psi(\zeta)$) corresponding to each dislocation is oriented along the slip plane and obeys the periodicity of the distribution. This is most conveniently done by developing the fields for pairs of dislocations on a glide plane, so that the displacement jump is between the dislocations. We have not been able to give a simple expression for the integration constant for all glide plane orientations, but have incorporated this in the numerical code for the evaluation of the displacement fields.

References

Acharya, A., Bassani, J.L., 2000. Incompatibility and crystal plasticity. J. Mech. Phys. Solids 48, 1565–1595.

Aifantis, E.C., 1984. On the microstructural origin of certain inelastic models. Trans. ASME J. Engng. Mater. Technol. 106, 326–330.

Armstrong, R., Codd, I., Douthwaite, R.M., Petch, N.J., 1962. The plastic deformation of polycrystalline aggregates. Philos. Mag. 7, 45–57.

Ashby, M.F., 1970. The deformation of plastically non-homogeneous materials. Philos. Mag. 21, 399–424.

Bassani, J.L., Needleman, A., Van der Giessen, E., 2001. Plastic flow in a composite: a comparison of nonlocal continuum and discrete dislocation predictions. Int. J. Solids Struct 38, 833–853.

Busso, E.P., Meissonnier, F.T., O'Dowd, N.P., 2000. Gradient-dependent deformation of two-phase single crystals. J. Mech. Phys. Solids 48, 2333–2361.

Cleveringa, H.H.M., Van der Giessen, E., Needleman, A., 1997. Comparison of discrete dislocation and continuum plasticity predictions for a composite material. Acta Mater. 45, 3163–3179.

Cleveringa, H.H.M., Van der Giessen, E., Needleman, A., 1999. A discrete dislocation analysis of bending. Int. J. Plast. 15, 837–868.

Cleveringa, H.H.M., Van der Giessen, E., Needleman, A., 2000. A discrete dislocation analysis of mode I crack growth. J. Mech. Phys. Solids 48, 1133–1157.

Fleck, N.A., 1991. Brittle fracture due to an array of microcracks. Proc. Roy. Soc. London A 432, 55–76.

Fleck, N.A., Hutchinson, J.W., 1993. A phenomenological theory for strain gradient plasticity. J. Mech. Phys. Solids 41, 1825–1857.

Fleck, N.A., Hutchinson, J.W., 1997. Strain gradient plasticity. Adv. Appl. Mech. 33, 295–361.

Fleck, N.A., Muller, G.M., Ashby, M.F., Hutchinson, J.W., 1994. Strain gradient plasticity: theory and experiment. Acta Metall. Mater. 42, 475–487.

Freund, L.B., 1994. The mechanics of dislocations in strained-layer semiconductor-materials. Adv. Appl. Mech. 30, 1–66.

Gao, H., Huang, Y., Nix, W.D., Hutchinson, J.W., 1999. Mechanism-based strain gradient plasticity – I. Theory. J. Mech. Phys. Solids 47, 1239–1263.

Gulluoglu, A.N., Srolovitz, D.J., LeSar, R., Lomdahl, P.S., 1989. Dislocation distributions in two dimensions. Scripta Metall. 23, 1347–1352.

Gurtin, M., 2000. On plasticity of crystals: free energy, microforces, plastic strain gradients. J. Mech. Phys. Solids 48, 989–1036.

Hansen, N., 1985. Polycrystalline strengthening. Metall. Trans. 16A, 2167–2190.

Hirth, J.P., Lothe, J., 1968. Theory of Dislocations. McGraw-Hill, New York.

Huang, Y., Gao, H., Nix, W.D., Hutchinson, J.W., 2000. Mechanism-based strain gradient plasticity – II. Analysis. J. Mech. Phys. Solids 48, 99–128.

Hughes, D.A., Hansen, N., 1993. Microstructural evolution in nickel during rolling from intermediate to large strains. Metall. Trans. A 24, 2021–2037.

Hutchinson, J.W., 2000. Plasticity at the micron scale. Int. J. Solids Struct. 37, 225–238.

Kubin, L.P., Canova, G., Condat, M., Devincre, B., Pontikis, V., Bréchet, Y., 1992. Dislocation microstructures and plastic flow: a 3D simulation. Solid State Phenom. 23 & 24, 455–472.

Mughrabi, H., 1983. Dislocation wall and cell structures and long-range internal stresses in deformed metal crystals. Acta Metall. 31, 1367–1379.

Muskhelishvili, N.I., 1953. Some Basic Problems of the Mathematical Theory of Elasticity. Noordhoff, Leyden.

Nabarro, F.R.N., 1967. Theory of Crystal Dislocations. Oxford University Press, Oxford.

Ortiz, M., Repetto, E.A., Stainier, L., 2000. A theory of subgrain dislocation structures. J. Mech. Phys. Solids 48, 2077–2114.

Petch, N.J., 1953. The cleavage strength of polycrystals. J. Iron Steel Inst. London 174, 25–28.

Rao, S.I., Hazzledine, P.M., Dimiduk, D.M., 1995. Interfacial strengthening in semi-coherent metallic multilayers. Proceedings of MRS Symposium, vol. 362, pp. 67–77.

Shen, Y.-L., Suresh, S., He, M.Y., Bagchi, A., Kienzle, O., Rühle, M., Evans, A.G., 1998. Stress evolution in passivated thin films of Cu on silica substrates. J. Mater. Res. 13, 1928–1937.

Shu, J.Y., Fleck, N.A., 1999. Strain gradient crystal plasticity: size-dependent deformation of bicrystals. J. Mech. Phys. Solids 47, 297–324.

Sun, S., Adams, B.L., King, W.E., 2000. Observations of lattice curvature near the interface of a deformed aluminium bicrystal. Philos. Mag. A 80, 9–25.

Van der Giessen, E., Needleman, A., 1995. Discrete dislocation plasticity: a simple planar model. Model. Simul. Mater. Sci. Engng. 3, 689–735.